JGR Solid Earth

RESEARCH ARTICLE
10.1029/2020JB021474

Seismic Diffraction Imaging to Characterize Mass-Transport Complexes: Examples From the Gulf of Cadiz, South West Iberian Margin

Jonathan Ford[1,2], **Roger Urgeles**[3], **Angelo Camerlenghi**[1], **and Eulàlia Gràcia**[3]

[1]National Institute of Oceanography and Applied Geophysics - OGS, Sgonico, Trieste, Italy, [2]Dipartimento di Matematica e Geoscienze, Università degli Studi di Trieste, Trieste, Italy, [3]Institut de Ciències del Mar, CSIC, Barcelona, Catalonia, Spain

Key Points:

- Seismic diffractions encode information about the small-scale internal structure of mass-transport complexes (MTCs)
- Diffraction images offer a low-cost route to improve the lateral resolution and effective vertical resolution of seismic images of MTCs
- 2D seismic profiles record out-of-plane diffractions generated by MTCs, which may be used to put minimum constraints on their 3D geometry

Supporting Information:

- Supporting Information S1

Correspondence to:
J. Ford,
jford@inogs.it

Citation:
Ford, J., Urgeles, R., Camerlenghi, A., & Gràcia, E. (2021). Seismic diffraction imaging to characterize mass-transport complexes: Examples from the Gulf of Cadiz, South West Iberian Margin. *Journal of Geophysical Research: Solid Earth*, *126*, e2020JB021474. https://doi.org/10.1029/2020JB021474

Received 2 DEC 2020
Accepted 17 JAN 2021

Abstract Mass-transport complexes (MTCs) are often characterized by small-scale discontinuous internal structure, such as slide blocks, rough interfaces, faults, and truncated strata. Seismic images may not properly resolve such structure because seismic reflections are fundamentally limited in lateral resolution by the source bandwidth. The relatively weak seismic diffractions, instead, encode information on subwavelength-scale structure, with superior illumination. In this paper, we compare diffraction imaging to conventional, full-wavefield seismic imaging to characterize MTCs. We apply a seismic diffraction imaging workflow based on plane-wave destruction filters to two 2D marine multichannel seismic profiles from the Gulf of Cadiz. We observe that MTCs generate a large amount of diffracted energy relative to the unfailed confining sediments. The diffraction images show that some of this energy is localized along existing discontinuities imaged by the full-wavefield images. We demonstrate that, in combination with full-wavefield images, diffraction images can be utilized to better discriminate the lateral extent of MTCs, particularly for thin bodies. We suggest that diffraction images may be a more physically correct alternative to commonly used seismic discontinuity attributes derived from full-wavefield images. Finally, we outline an approach to utilize the out-of-plane diffractions generated by the 3D structure of MTCs, normally considered a nuisance in 2D seismic processing. We use a controlled synthetic test and a real-data example to show that under certain conditions these out-of-plane diffractions might be used to constrain the minimum width of MTCs from single 2D seismic profiles.

Plain Language Summary Underwater landslides are a significant geohazard that can generate large magnitude tsunami and threaten seafloor infrastructure such as pipelines and telecommunication cables. The deposits from these events (so-called mass-transport complexes, or MTCs) can preserve internal structure that can reveal the dynamics of failure, important to understanding the geohazard potential of future events. One common tool for investigating these deposits is seismic imaging, which uses recordings of seismic waves reflected and scattered from the subsurface to image the geology. The resolution of the reflected waves, however, is often too poor to properly characterize the complex, strongly deformed internal structure of MTCs. In this study, we instead use the seismic waves scattered at lateral, basal, and internal discontinuities formed by landslide processes to produce diffraction images of MTCs. We show that these images have improved resolution and illumination of the small-scale structure. We suggest that diffraction imaging could be a useful tool for geohazard investigations of complex geology.

1. Introduction

Mass-transport complexes (MTCs) are the deposits of subaqueous mass-movements such as debris flows, slides, and slumps (Mulder & Cochonat, 1996; Piper et al., 1997; Prior et al., 1984; Sawyer et al., 2009). Such events pose a significant geohazard to coastal populations from landslide-induced tsunami (Satake, 2012; Tappin et al., 2001) and to seafloor infrastructure such as telecommunications cables and pipelines (Carter et al., 2014; Piper et al., 1999). MTCs have important implications for hydrocarbon exploration as they form a significant proportion of deepwater sediment fill (Weimer & Shipp, 2004) and they can have both reservoir and seal potential (Alves et al., 2014; Cardona et al., 2016). They also represent a drilling hazard as they are often overconsolidated (densified) compared to unfailed sediments (Shipp et al., 2004).

MTCs can preserve complex, laterally discontinuous internal structure such as slide blocks, rough interfaces, faults, and truncated strata (Bull et al., 2009; Lucente & Pini, 2003). These so-called *kinematic indicators* can record the dynamics of failure, transport, and emplacement, important for constraining the flow type and the geohazard potential of future mass-movements. When the scale of this structure is close to the limit of seismic resolution, seismic images of MTCs can be difficult to interpret, often showing an apparently "chaotic" or "disordered" seismic character (Posamentier & Martinsen, 2011). This can be a problem when discriminating between different types of mass-movements, for example, debris flow deposits (lacking internal bedding, chaotic seismic character) and slumps (internal bedding preserved but may still show a chaotic seismic character without sufficient seismic resolution). This can also make it difficult to characterize the amount and style of deformation within a deposit.

Efforts to improve the characterization of internal structure from seismic images have largely relied on improvements in acquisition technology in recent decades. Industry-scale 3D seismic surveys can provide the spatial resolution and coverage to observe large-scale internal structure within MTCs, particularly from plan-view time and depth slices (e.g., Bull et al., 2009; Frey Martinez et al., 2005; Gafeira et al., 2010; Lackey et al., 2018; Steventon et al., 2019). In academic settings, maximum offsets are typically limited relative to the target depth, meaning reflectors are often poorly illuminated, intrinsically limiting the lateral resolution. Improvements in imaging of academic data have typically come from novel acquisition geometries and seismic sources, such as ultra-high-resolution deep-tow seismic (Badhani et al., 2020) and short-offset 3D "P-cable"-type geometries (Berndt et al., 2012; Karstens et al., 2019). Such approaches can provide dramatic increases in seismic resolution within MTCs at the cost of significantly increased acquisition effort.

An alternative strategy to improve the interpretable resolution of existing seismic data is to apply quantitative interpretation techniques such as seismic attributes (Chopra & Marfurt, 2007). Seismic attributes can highlight discontinuities and identify areas of disrupted seismic reflectors by deriving statistical properties within data windows of seismic images. Such approaches have been applied to discriminate MTCs from background sedimentation (when they have chaotic internal seismic character) as well as to characterize the flow direction and assess the degree of internal disaggregation (e.g., Alves et al., 2014; Bhatnagar et al., 2019). Seismic attributes, however, are typically derived from full-wavefield seismic images, which suffer from the lateral resolution limits outlined above, and data windowing can reduce their effective resolution with respect to the original image.

Conventional seismic processing emphasizes preserving and imaging the reflected seismic wavefield—the relatively weak diffracted wavefield is often ignored, aliased, or accidentally attenuated (Klem-Musatov et al., 2016; Schwarz, 2019b). Seismic reflections cannot properly resolve geological structures smaller than the Rayleigh limit (i.e., half a seismic wavelength; on the order of meters to decameters for typical marine airgun data) (Born & Wolf, 1959; Chen & Schuster, 1999). Such structures, instead, scatter the seismic waves and generate diffractions, meaning that the diffracted wavefield can encode subwavelength information about small-scale subsurface discontinuities. Diffraction imaging works by separating the reflected and diffracted wavefields and migrating only the diffracted component, producing an image of these small-scale heterogeneities (Klem-Musatov et al., 2016; Schwarz, 2019b). Contrary to reflections, the radiation pattern of diffractions is independent of the dip (Figure 1), meaning that they can be fully illuminated even by short-offset or zero-offset receiver arrays (Preine et al., 2020). Combined with the general smaller scale of diffractors compared to reflectors, this radial spreading means that for a given seismic source the recorded diffracted wavefield tends to be significantly weaker and have higher frequency content than the reflected wavefield. Consequently, the relatively high-amplitude, long-wavelength reflections can easily mask the diffractions in conventional, full-wavefield seismic images. Therefore diffraction images offer potentially improved lateral resolution and better illumination of small-scale, discontinuous geological structure. Several approaches for diffraction separation have been developed. Some exploit the difference in moveout of reflections and diffractions in common-shot or common-midpoint (CMP) domains (Khaidukov et al., 2004), or the difference in dip and lateral continuity between reflections and diffractions in common-offset domain (Decker et al., 2017; Fomel et al., 2007; Taner et al., 2006). Others rely on wavefront attributes and the assumed coherence of seismic reflections to model and subtract the reflected wavefield (Dell & Gajewski, 2011; Schwarz & Gajewski, 2017). Another approach is to perform the separation during migration, exploiting the fact that diffractions in migrated dip-angle domain appear flat, whereas reflections appear as hyperbolae (Moser & Howard, 2008).

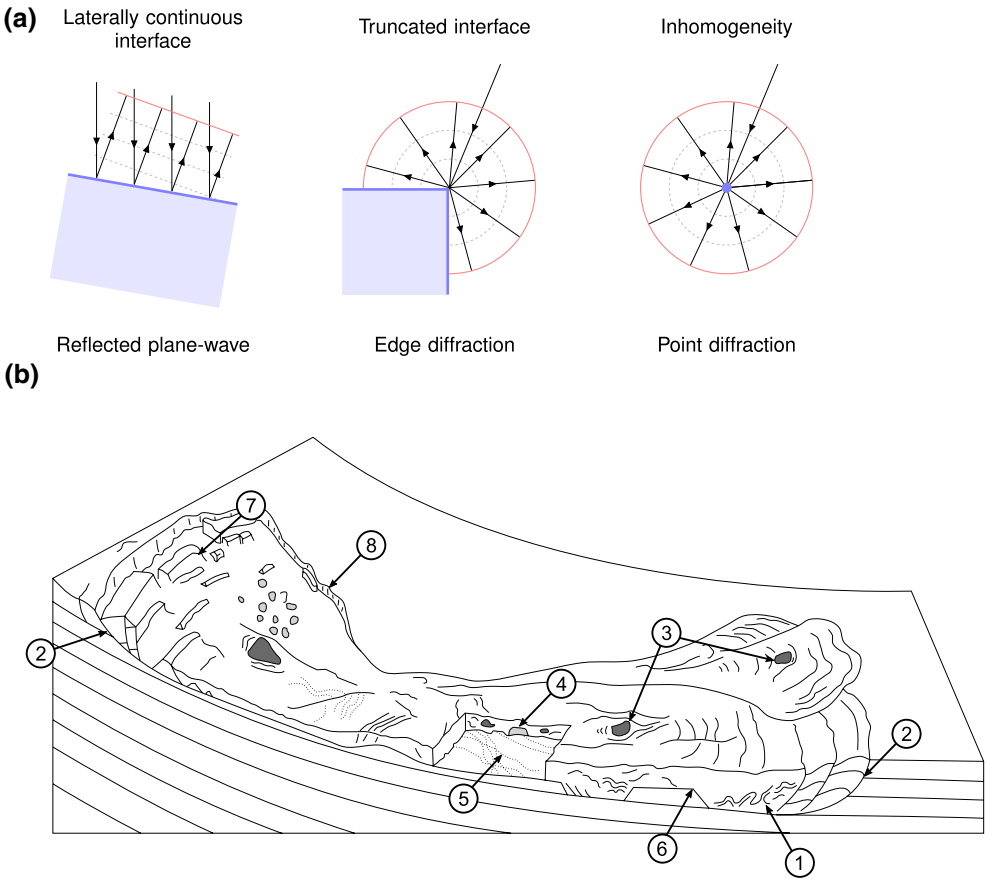

Figure 1. (a) The 2D radiation pattern of reflections from a laterally continuous interface compared to diffractions from truncations (infinite curvature *edge diffractors*) or subwavelength-scale heterogeneities (*point diffractors*). (b) Schematic diagram of a mass-transport complex labeled with discontinuous structure likely to generate seismic diffractions: (1) intense folding; (2) extensional and compressional shear zones; (3) transported clasts; (4) boundaries of slide blocks; (5) rough basal topography; (6) ramp-and-flat structures; (7) headwall scarps; and (8) lateral margins (modified from Bull et al. (2009)).

MTCs very often contain a large amount of potential diffractors: interfaces with width below the Rayleigh criterion (subwavelength-scale heterogeneities) or near-infinite local curvature (edges, discontinuities, and truncations) (Figure 1). Examples of such internal structure could include the hinges of slump folds (Alsop & Marco, 2013); offset across normal and reverse faults within extensional and compressional shear zones (Posamentier & Martinsen, 2011); wavelength-scale transported clasts (Talling et al., 2010); truncated reflectors at the boundaries of slide blocks (Sobiesiak et al., 2016); rough basal topography and ramp-and-flat structures (Lucente & Pini, 2003); headwall scarps (Bull et al., 2009); and steep, erosive lateral margins (Frey Martinez et al., 2005). This points to the potential of seismic diffractions to encode unique information on the small-scale internal structure and the discontinuous external boundaries of MTCs. Indeed, the presence of diffraction tails (sometimes referred to as *hyperbolae*, although diffractions are only strictly hyperbolic when the overburden velocity structure is laterally homogeneous) in unmigrated seismic and subbottom profiler data is often used as an indicator of mass-movements (Diviacco et al., 2006; Urgeles et al., 1999). Even MTCs that do preserve coherent, well-imaged internal strata or internal geometry may benefit from the superior illumination of diffractions, especially at the discontinuous basal surface, lateral margins, and internal dislocation planes between slide blocks. Structural reconstruction to quantify strain distribution within MTCs relies on the proper imaging of such supraseismic scale interfaces (Bull & Cartwright, 2020; Steventon et al., 2019).

Seismic diffraction imaging has been used to characterize a range of complex geological targets including faults, channels, pinchouts, rugose interfaces, karstic carbonate reservoirs, and fracture zones (Decker

et al., 2015; Fomel et al., 2007; Reshef & Landa, 2009; Schwarz & Krawczyk, 2020). In this paper, we explore the potential of diffraction imaging to characterize the complex internal structure and external morphology of MTCs. This approach has the potential to increase the value of existing seismic data during processing at relatively low additional computational cost (comparable to a conventional migration). We apply diffraction imaging to two 2D, multichannel seismic profiles containing prominent MTCs from the Gulf of Cadiz (south west Iberian Margin). We first demonstrate the ability of diffraction images to resolve small-scale internal structure compared to conventional, full-wavefield seismic images. We then compare diffraction images to traditional seismic discontinuity attributes for identification and interpretation of relatively small, thin MTCs. Finally, we outline a speculative approach to utilize the illumination of out-of-plane diffractions (normally considered a nuisance) and the inherently 3D structure of MTCs. We suggest that in certain conditions this out-of-plane diffracted energy might be used to constrain the minimum cross-line width of MTCs from single 2D seismic profiles.

2. Geological Setting

The Gulf of Cadiz is located offshore the south west margin of the Iberian Peninsula and north west Morocco (Figure 2). The region is characterized by active tectonics related to convergence between the African and Eurasian plates. The tectonic structure and seafloor morphology of the gulf is the result of an accretionary wedge formed from the Late Cretaceous to the Late Miocene (Zitellini et al., 2009). The accretionary wedge is covered by Late Miocene to Plio-Quaternary sediments, pierced by mud volcanoes and pockmarks (indicating active fluid flow) and salt diapirs (Gràcia, Dañobeitia, Vergés, Bartolomé, et al., 2003; Gràcia, Dañobeitia, Vergés, & PARSIFAL Team, 2003; Medialdea et al., 2009; Zitellini et al., 2009). The Gulf of Cadiz and the south west Iberian Margin host large magnitude ($M_w > 8$) earthquakes (Gràcia et al., 2010; Matias et al., 2013) and submarine landslides (Urgeles & Camerlenghi, 2013). Both processes pose significant tsunami hazard to nearby coastal populations (Baptista & Miranda, 2009; Leynaud et al., 2017; Lo Iacono et al., 2012). This study uses geophysical data collected from two areas of the Gulf of Cadiz: the Portimão Bank and the Infante Don Henrique Basin.

The Portimão Bank is an east-west trending tectonic high located south of Portugal, at the external part of the Gulf of Cadiz. The area is characterized by bottom currents and contourite deposition associated with the Mediterranean Outflow Water (Brackenridge et al., 2013) and mass-movements (slides and slide scars; Silva et al., 2020). Salt diapirs pierce the shallow Plio-Quaternary sediments and the corresponding doming is evident in the bathymetry (Figure 2b). The rapid deposition of poorly consolidated contourites and slope steepening from salt diapirism are primary preconditioning factors for mass-failure, evidence of which is widespread in the area (Mulder et al., 2009; Silva et al., 2020).

The Infante Don Henrique Basin is located at the south west of the Cape São Vicente (Figure 2). It is bound on its eastern side by the Marquês de Pombal fault, a ~55-km long, north-south trending, active reverse thrust fault (Gràcia, Dañobeitia, Vergés, Bartolomé, et al., 2003; Terrinha et al., 2003; Zitellini et al., 2004). The fault is expressed in the bathymetry as a monocline, with water depth rapidly increasing from the hanging wall block (2,000 m water depth) to the basin located in the footwall block (3,900 m water depth). A succession of stacked MTCs is preserved in the Plio-Quaternary deposits in the basin, likely recording recent seismic activity of the fault (Gràcia et al., 2010; Vizcaino et al., 2006), which has been considered as a potential source of the $M_w > 8$ 1755 Lisbon earthquake (Baptista et al., 1998; Terrinha et al., 2003). Recent mass-failure events are also visible in the bathymetry of the steeply dipping hanging wall block (Figure 2c). Preconditioning factors for mass-failure in the area include slope steepening of the advancing thrust front and potential excess pore pressure related to the relatively high sedimentation rate and lateral fluid flow. Near-field seismic activity along the Marquês de Pombal fault is likely a primary trigger mechanism for some of the mass-failure events, as well as far-field seismicity from the rest of the Gulf of Cadiz.

3. Data and Methods

3.1. Geophysical Data

This study uses two 2D marine multichannel seismic reflection profiles from the Gulf of Cadiz acquired during the INSIGHT (Imaging large seismogenic and tsunamigenic structures of the Gulf of Cadiz

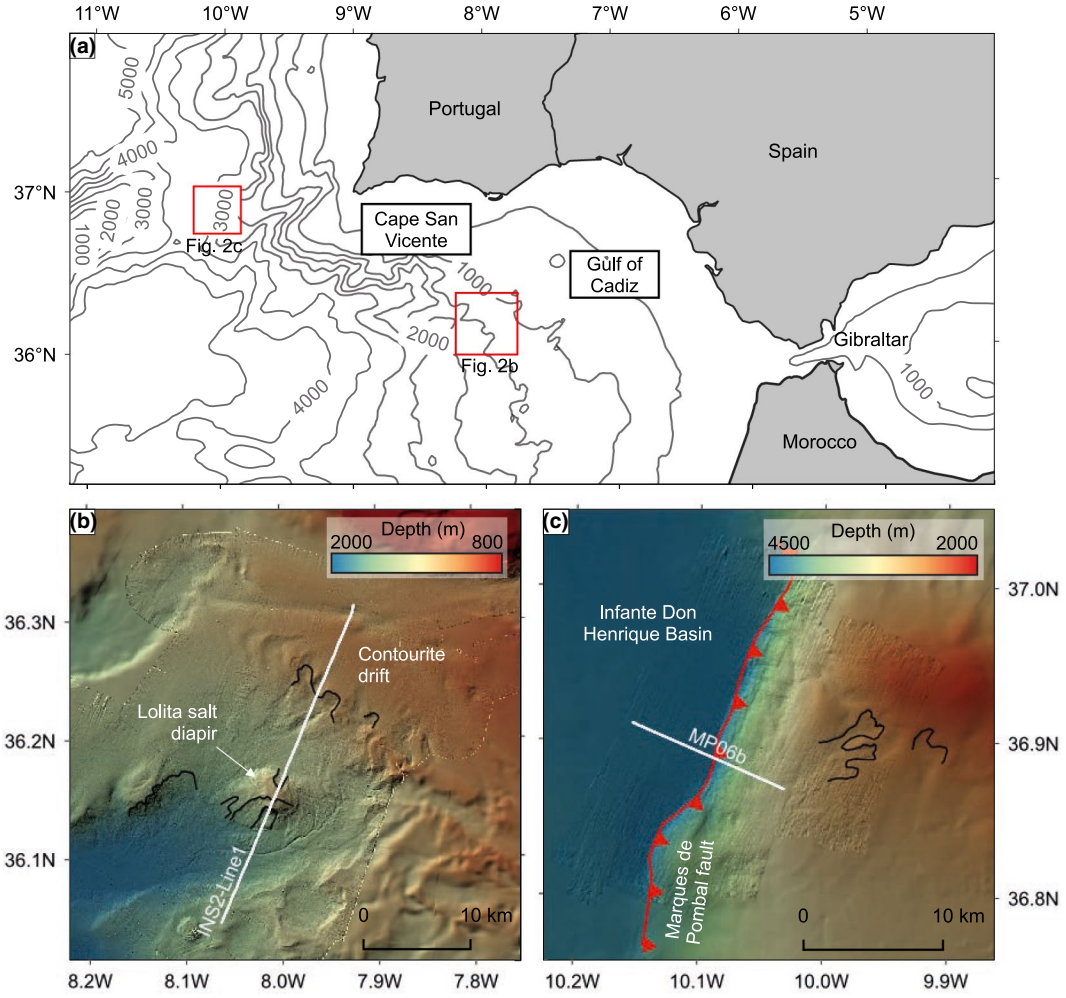

Figure 2. (a) Overview map of the Gulf of Cadiz and surroundings, with bathymetric contours (500 m interval). (b) Bathymetry of Portimão Bank area, location of seismic profile INS2-Line1 indicated. (c) Bathymetry of Infante Don Henrique Basin area, location of Marquês de Pombal fault trace at the seafloor (after Gràcia, Dañobeitia, Vergés, & PARSIFAL Team, 2003) and seismic profile MP06b indicated. Headscarps from mass-movements are shown as black lines.

with ultra-high-resolution technologies) cruises in May 2018 (Leg 1) and October 2019 (Leg 2) (Gràcia et al., 2018; Urgeles et al., 2019).

The seismic acquisition and processing flow were designed to maximize the temporal and spatial resolution of the resulting seismic images. The shot interval was chosen to ensure a nominal coverage of at least 12-fold with a midpoint interval of 3.125 m. A relatively small seismic source (an airgun array with total volume 930 $in.^3$) was used to maximize the dominant source frequency. The source array and streamer were towed at a relatively shallow depth (~3 m) to ensure that the frequency of the first source and receiver ghost notches were as high as possible. Broadband preprocessing was performed onboard using RadExPro seismic processing software. Traditional preprocessing focuses on imaging specular reflections, meaning that diffractions are often ignored or removed, particularly by processes that target dipping energy, such as τ–p and f–k filters. Preserving diffractions through the preprocessing flow requires care as they are generally lower amplitude, higher frequency, and dip more steeply compared to reflections. The broadband preprocessing flow consisted of (i) swell noise removal (to enhance the signal-to-noise ratio at low frequencies); (ii) deghosting (to correct for the source and receiver ghost effect, enhancing the bandwidth); (iii) designature (to transform the data to zero-phase and remove the bubble pulse, boosting the low frequency content); and (iv) shot domain τ–p muting (to remove steeply dipping noise, taking care to preserve the diffractions). For most

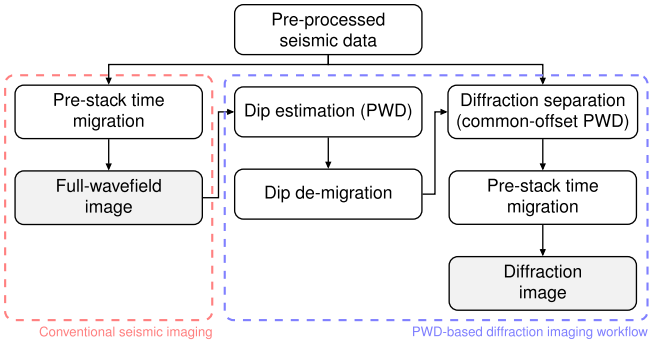

Figure 3. Comparison of workflows for conventional full-wavefield seismic imaging and the plane-wave destruction (PWD) filter-based diffraction separation and imaging workflow used in this study. The dip field is estimated from the migrated full-wavefield image, then demigrated using the migration velocities, giving the dominant slope of the unmigrated reflections (Appendix A). This is used to guide the PWD filter for diffraction separation.

of the survey area, the signal penetration depth was similar to, or less than, the two-way travel time (TWTT) of the first waterbottom multiple, therefore no multiple attenuation was performed. Instead, a bottom-mute was applied from above the first waterbottom multiple before imaging to prevent high-amplitude multiple energy from migrating upwards into the shallow section as noise. Full details of the acquisition and preprocessing parameters for both profiles are given in the supplementary information (Tables S1 and S2). The signal bandwidth of the migrated full-wavefield images is approximately 8–250 Hz (range estimated from the amplitude spectrum of a window around the waterbottom reflection, 20 dB below the peak amplitude).

3.2. Diffraction Separation

This study uses a dip-guided plane-wave destruction (PWD) filter approach for diffraction separation on unmigrated data, modified to be robust to high-amplitude diffractions and steeply dipping reflections present in the example profiles from the Gulf of Cadiz. Figure 3 shows an outline of the diffraction imaging workflow compared to a conventional full-wavefield seismic imaging workflow.

The recorded seismic wavefield can be considered as the superposition of (i) reflected energy, (ii) diffracted energy, and (iii) noise (including other seismic arrivals, such as multiples). When the noise is low, the diffracted wavefield can be retrieved by subtracting the reflected wavefield from the recorded wavefield. In this study, we perform the separation using a dip-guided PWD filter approach in the time domain on common-offset gathers (as in, e.g., Decker et al., 2017; Fomel et al., 2007). This approach assumes that reflections are locally planar events in common-offset domain (Harlan et al., 1984). PWD filters calculate the dominant local slope by following energy between traces and iteratively minimizing the residual energy (Claerbout, 1992; Fomel, 2002). The residual energy contains the diffracted energy and noise, with laterally coherent events with continuous local slope (i.e., smooth) that are close to the estimated dominant slope (the apparent dip of the unmigrated reflectors) eliminated.

The PWD filter is guided by an estimate of the dominant slope (dip). Robust diffraction separation therefore depends on accurate estimation of the dominant slope of the *unmigrated* reflections. Due to the general rough topography of the seafloor in the Gulf of Cadiz, the example profiles in this study contain a large number of high energy diffractions with similar amplitude to major reflections. In addition, some reflections are steeply dipping, often subparallel to the diffraction tails. This prevents accurate estimation of the dominant slope of the reflectors directly from the unmigrated data (as in, e.g., Fomel et al., 2007). We instead estimate the dip field from the migrated full-wavefield image, where diffractions are collapsed and the continuity of reflections enhanced. Using the migration velocities, we then demigrate this dip field to estimate the dominant slope of the unmigrated reflections. Details of the dip demigration algorithm are given in Appendix A.

3.3. Imaging

Diffractions, like reflections, can be imaged by Kirchhoff-type migrations, in both time and depth domains (Moser & Howard, 2008). For this study, the real-data examples are migrated using a 2D prestack Kirchhoff time migration (Fomel et al., 2013; Lumley et al., 1994), with a migration aperture limited to 60°. Identical migrations are performed for the full-wavefield and diffraction images so that the geometry of both images is comparable (Figure 3). The diffraction images in this study are presented as the energy (squared envelope) of the diffraction image (as in, e.g., Preine et al., 2020).

A classic application for diffraction imaging is to derive migration velocity fields by focusing analysis of the diffracted wavefield (e.g., Decker et al., 2017; Fomel et al., 2007; Preine et al., 2020). Under the correct migration velocity, diffractions will collapse (focus) to a point at their apex. The example 2D profiles in this study both contain significant contributions from out-of-plane diffractions around the target MTCs and

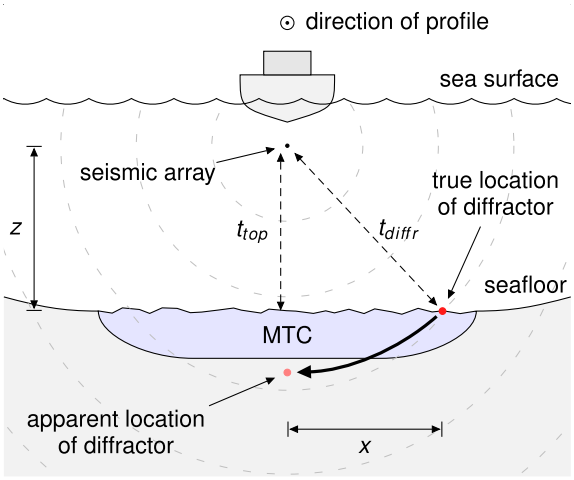

Figure 4. Conceptual diagram oriented perpendicular to a 2D seismic profile showing how an out-of-plane diffractor at the seafloor will appear to "swing" into the plane of the profile. The seismic source and receiver arrays (seismic datum) and the expanding seismic wavefront are marked. x and z are the horizontal offset and depth of the diffractor with respect to the seismic array. t_{top} and t_{diffr} are the two-way travel times to the top of the mass-transport complex (MTC) and to the diffractor.

from the rugose seafloor (Section 3.4). Out-of-plane diffractions will not be properly focused by 2D migration, so their presence biases the derived migration velocity fields. As a consequence, we were not able to obtain plausible migration velocities from focusing–defocusing analysis of the diffracted wavefield in these examples. A more traditional method for migration velocity analysis is to pick velocity trends from semblance panels of migrated CMP gathers. This method relies on the approximately hyperbolic moveout of seismic reflections with offset. The example 2D profiles in this study were acquired with a relatively short streamer, giving a low far-offset (hundreds of meters) with respect to the depth of the target MTCs (kilometers). Consequently, there was not great enough differential moveout between reflections to perform an accurate and robust semblance velocity analysis.

Instead, the migration velocity fields used in this study were derived during onboard processing as a constant velocity in the water column and a velocity gradient in the sediments. The postmigration waterbottom horizon was picked on a near-offset section migrated with a water velocity Stolt migration (Stolt, 1978). The optimal sediment velocity gradients were estimated for each area by generating an ensemble of images migrated with a range of gradients and choosing the gradient that appeared to best focus reflections and diffractions for all profiles in an area. The sediment velocity gradient is then inserted below the smoothed postmigration waterbottom horizon to make the migration velocity field. For seismic profiles INS2-Line1 and MP06b, the optimal sediment velocity gradient was estimated during onboard processing as 200 and 125 m s^{-2}, respectively (Gràcia et al., 2018; Urgeles et al., 2019). The water velocity for both profiles is 1,500 m s^{-1}. The resulting migration velocity fields are presented in the supplementary information (Figure S5). These migration velocities are considered reasonable at the target depths because the MTCs in these examples are close to the seafloor (with respect to the water depth) and both the reflection and diffraction images appear to be generally well focused. An analysis of the sensitivity of diffraction imaging to the migration velocities is presented in the supplementary information (Figure S7).

3.4. Constraining the Location of Out-of-Plane Diffractors

For 2D seismic profiles, out-of-plane energy (i.e., seismic energy reflected and scattered from interfaces outside the vertical plane of the profile) can contaminate the image. The illumination of seismic reflectors depends on the local dip of the reflector and the geometry of the receiver array. Diffractions, however, are 3D phenomena, fully illuminated from all angles even by single-channel, zero-offset data (Figure 1a and Preine et al., 2020). This means that 2D diffraction images will suffer more strongly from out-of-plane energy than corresponding 2D reflection images. Out-of-plane energy is usually regarded as a source of noise in 2D seismic profiles, as it cannot be properly migrated and interferes with in-plane primary energy.

We suggest that these out-of-plane diffractions, under certain strong assumptions, may provide a source of information about the 3D geometry of MTCs from 2D profiles. MTCs are inherently 3D geobodies (Figure 1b), so 2D seismic images of MTCs will, in general, suffer more strongly from out-of-plane energy than 2D seismic images of unfailed sediments. Therefore, we expect *diffraction images* of MTCs from 2D seismic profiles to contain particularly large contributions from out-of-plane energy.

The apparent TWTT of an out-of-plane diffractor, t_{diffr}, can be predicted from the cross-line distance to the diffractor, x, the depth of the diffractor below the seismic datum, z, and the average velocity along the raypath from the seismic array to the diffractor, v_{rms} (Figure 4):

$$t_{diffr} = \frac{2\sqrt{x^2 + z^2}}{v_{rms}}. \quad (1)$$

If diffractors are distributed throughout the MTC, some of the recorded diffraction energy will always come from *outside* the vertical plane of the profile (i.e., $|x| > 0$ in Figure 4). If the body is wider than it is thick and contains abundant diffractors, the apparent thickness of the slide from diffraction images will be greater than the apparent thickness of the slide from reflection images. This results in a "shadow" of diffraction energy below the true basal surface of the MTC in 2D diffraction images. From Equation 1, it follows that the thickness of this diffraction shadow is related to the half-width, perpendicular to the profile, of the zone of out-of-plane diffractors that contribute to the image. We propose that this could provide a minimum bound on the cross-line half-width of an MTC (i.e., relate the zone where out-of-plane diffractions could originate to the geometry of an MTC) under certain (strong) assumptions:

1. *Diffractors spread throughout body*. Diffractors are widespread inside the body compared to outside the body, where there are relatively fewer diffractors.
2. *Known top surface*. The top surface of the MTC must be assumed. In practice, this can often be well constrained by bathymetry (for bodies at the seafloor) or reasonably assumed to be constant depth perpendicular to the profile.
3. *Thin body*. The thickness of the body is small relative to its depth, meaning that all diffractors can be treated as if they are at the assumed top surface.
4. *Laterally homogeneous overburden velocity*. Equation 1 assumes a straight raypath to the true location of the diffractor, implying that the overburden velocity, v_{rms}, is constant in a cross-line direction, even if the water depth changes.
5. *Distinct diffraction shadow*. The diffraction shadow is associated with a single body and can be clearly differentiated from the background and from other bodies that may also generate diffractions. The cross-line width is large enough with respect to the thickness that the diffraction shadow extends *below* the true basal reflector.

If these assumptions are satisfied, the diffraction shadow provides an estimate of the half-width of the zone containing the diffractors that swing into the profile. In other words, it places a lower bound on the width of an MTC from a single 2D seismic profile. Diffractions are relatively low amplitude seismic events, and their radiation pattern means that their amplitude depends strongly on the distance from the seismic array (Figure 1a). Therefore in practice this lower bound on the half-width from the diffraction shadow will generally be an underestimate of the true half-width.

3.4.1. Controlled Synthetic Demonstration

The aim of this synthetic test is to demonstrate that 3D information generated by a heterogeneous geobody is encoded in 2D seismic profiles by out-of-plane diffractions, producing a diffraction shadow. If the above assumptions are satisfied, the apparent TWTT to the base of the diffraction shadow can be related to the overall width of the geobody by Equation 1.

The 3D synthetic model has dimensions 500 m × 500 m × 500 m with a grid spacing of 1 m. The *P* wave velocity is constant, $v_p = 1{,}500$ m s^{-1}. The background density is constant, $\rho = 1{,}400$ kg m^{-3}, everywhere except for a half-ellipsoidal region representing an MTC in the center of the model. Inside the MTC zone are randomly located $n = 2{,}117$ point diffractors (single cells of higher density, $\rho = 3{,}000$ kg m^{-3}). The 3D, zero-offset seismic response is modeled using one-way wave extrapolation with an extended split-step scheme (Gazdag & Sguazzero, 1984; Kessinger, 1992) and a 50-Hz Ricker wavelet source signature. The modeled seismic volume, 3D migration, and 2D migration of a section through the diffractor zone are presented in Section 4.4.1.

3.4.2. Real-Data Demonstration

The aim of this real-data test is to demonstrate a practical workflow to assess the zone of out-of-plane diffractors that contribute to example seismic profile INS2-Line1. As MTC A is close to the seafloor, we can make the simplifying assumption that potential internal diffractors are at, or near, the seafloor (Section 3.3). This implies $v_{rms} \approx v_{water} = 1{,}500$ m s^{-1}. We also assume that the seafloor is equivalent to the potential top surface of the MTC. The seafloor depth is known independently from multibeam swath bathymetry (Figure 2).

The workflow to calculate the zone of diffractors that contribute to the image is as follows:

1. Pick the apparent base of the diffraction shadow associated with the MTC, t_{diffr}, from the diffraction image.
2. For each interpreted CMP location along the profile:
   (a) Compute the horizontal distance, x, from the CMP to each point on the seafloor.
   (b) For each point on the seafloor, compute the TWTT from the CMP to the potential top surface of the body, t_{top}, using Equation 1 with $v_{rms} = 1{,}500$ m s^{-1} and z equal to the depth of the seafloor.
   (c) Grid points with TWTT less than the interpreted base diffraction shadow ($t_{top} < t_{diffr}$) are considered potential locations for diffractors originating perpendicular to the profile at this CMP location.

4. Results

4.1. Diffraction Imaging

4.1.1. Profile INS2-Line1

The full-wavefield seismic image of the INS2-Line1 profile largely consists of parallel, high-amplitude reflectors interpreted to be of Plio-Quaternary age, pierced by the Lolita salt diapir, forming a ~4 km wide dome at the seafloor in the center of the profile (Figure 5). The doming has resulted in slope failures that radiate from the center of the dome, visible in the bathymetry (Figure 2b). To the north, the upper Late Quaternary sediments onlap and pinchout, which characterizes a major contourite drift deposit resulting from bottom currents associated with the Mediterranean Outflow Water. Three prominent MTCs, MTC A, MTC B, and MTC C, are clearly visible on the full-wavefield seismic image ((Figure 5a) and Figure 6a, a zoom on MTC A). MTC A and MTC B are both exposed at the seafloor, having in-profile lengths of ~7.4 km and ~3.7 km, respectively, and maximum in-profile thicknesses of ~95 ms TWTT and ~130 ms TWTT, respectively. MTC C is deeper, partly underlying MTC B, with an in-profile length of ~5.1 km and a maximum in-profile thickness of ~140 ms. MTC A originated from the drift deposits, whereas MTC B originated from the salt diapir. Both propagated toward the south. MTC C, instead, failed toward the north, in the direction of the salt diapir.

Figure 5b shows the unmigrated full-wavefield stack of INS2-Line1. Diffraction tails are visible originating from the rugose, high-amplitude seafloor and top salt interfaces. Figure 5c shows the estimated dominant slope of the unmigrated reflectors (demigrated dip field estimated from the full-wavefield seismic image) overlaid on the unmigrated stack. The dip estimate appears to follow the dip of the prominent horizons well.

Figure 5d shows a stack of the separated diffractions. This view is comparable to the unmigrated stack (Figure 5b). Diffraction tails are clearly seen throughout the section, including from (i) two zones of normal faults (CMPs 1500–3000 and 9100–10000); (ii) inside the prominent MTCs (CMPs 3000–5500 and 7000–9000); and (iii) within the deeper, chaotic unit (CMPs 1000–5000 and 9000–10000, below around 2.4 s). The diffraction image shows high amplitudes inside MTC A, MTC B, and MTC C, inside the smaller MTC D (below MTC A), at the rugose top salt interface and within the deeper chaotic unit (Figure 5e). Both zones of normal faults are remarkably well resolved compared to the full-wavefield image, where they are difficult to interpret due to their small offsets. Some residual reflection energy remains, particularly in areas of rapidly varying dip (see Figure 6, label "g").

4.1.2. Profile MP06b

The MP06b seismic profile is a cross-sectional view of the Marquês de Pombal fault (Figures 7 and 8). The profile can be divided into two main sections: the Infante Don Henrique Basin (the footwall of the Marquês de Pombal fault) and the steeply dipping slope area (the frontal part of the hanging wall of the fault). The full-wavefield seismic image shows that the Infante Don Henrique Basin contains a >1-s TWTT thick, stacked succession of MTCs with apparently chaotic to transparent seismic character, separated by parallel horizons representing the unfailed confining sediments (Figures 7a and 8a). The hanging wall of the Marquês de Pombal fault is more deformed—the shallow part of the slope shows extremely disordered, overlapping horizons reflecting the complex seafloor topography caused by mass-wasting in the slope area. The Marquês de Pombal fault plane is not directly imaged in these data; the fault zone is represented by a zone of relatively low amplitude, disordered reflectors dipping to the south east (CMPs 1900–2500, 5.25–6.5 s TWTT).

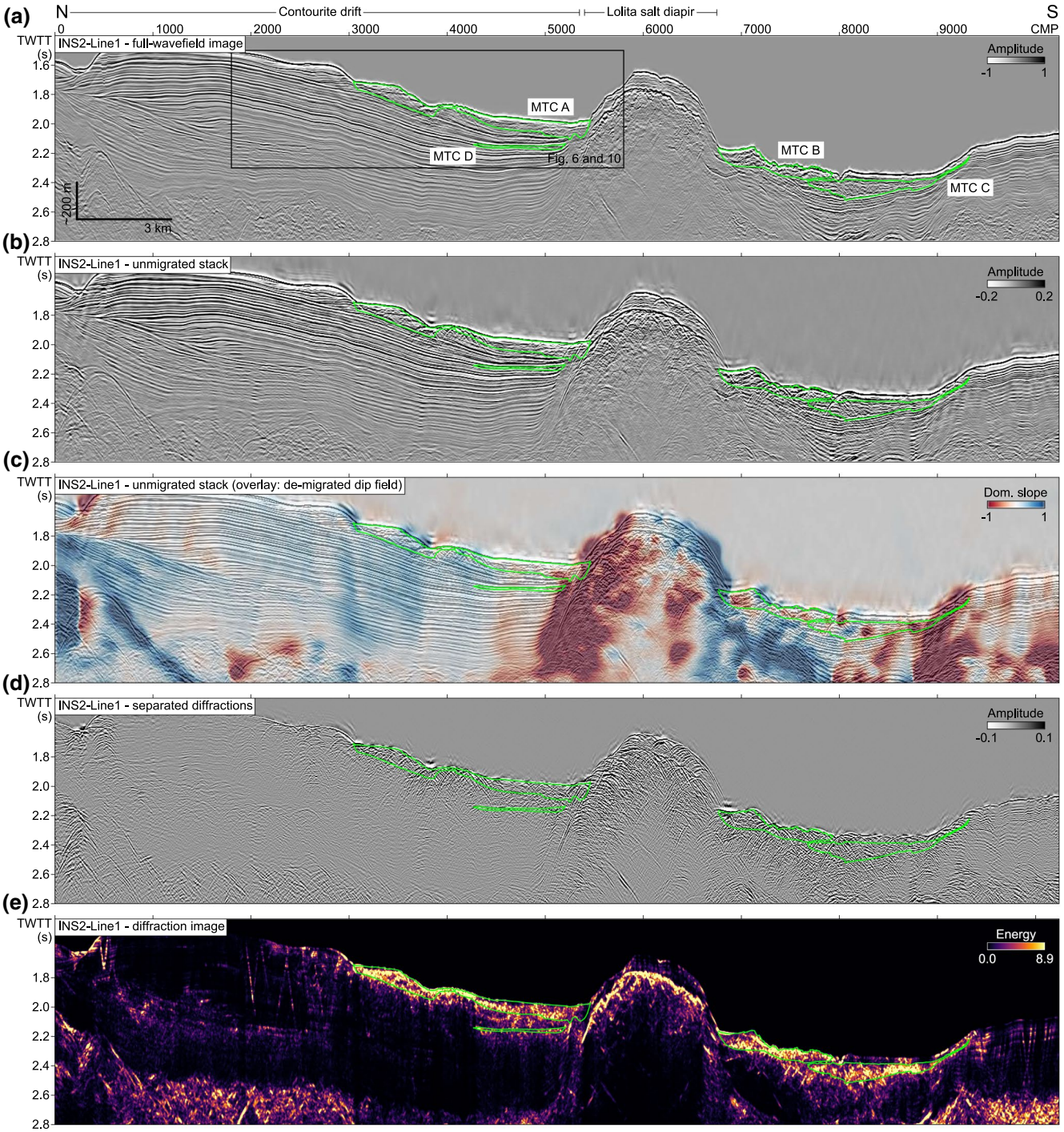

Figure 5. Seismic profile INS2-Line1 from the Portimão Bank area (Figure 2), mass-transport complexes (MTCs) outlined in green. (a) Full-wavefield migrated seismic image. (b) Unmigrated stacked conventional data (reflections and diffractions). (c) Demigrated estimated dip field (dominant slope of reflectors) overlaid on the unmigrated conventional stack. (d) Unmigrated stacked separated diffractions. (e) Diffraction image.

Figure 7b shows the unmigrated stack of MP06b. Diffraction tails are visible originating from the rugose seafloor in the steeply dipping hanging wall area (CMPs 1800–3000) and from truncated reflectors where the Infante Don Henrique Basin meets the low amplitude, disordered zone containing the Marquês de Pombal fault. Figure 7c shows the estimated dominant slope (demigrated dip field estimated from Figure 7a) overlaid on the unmigrated stack. In general, the dominant slope appears to follow the dip of the prominent

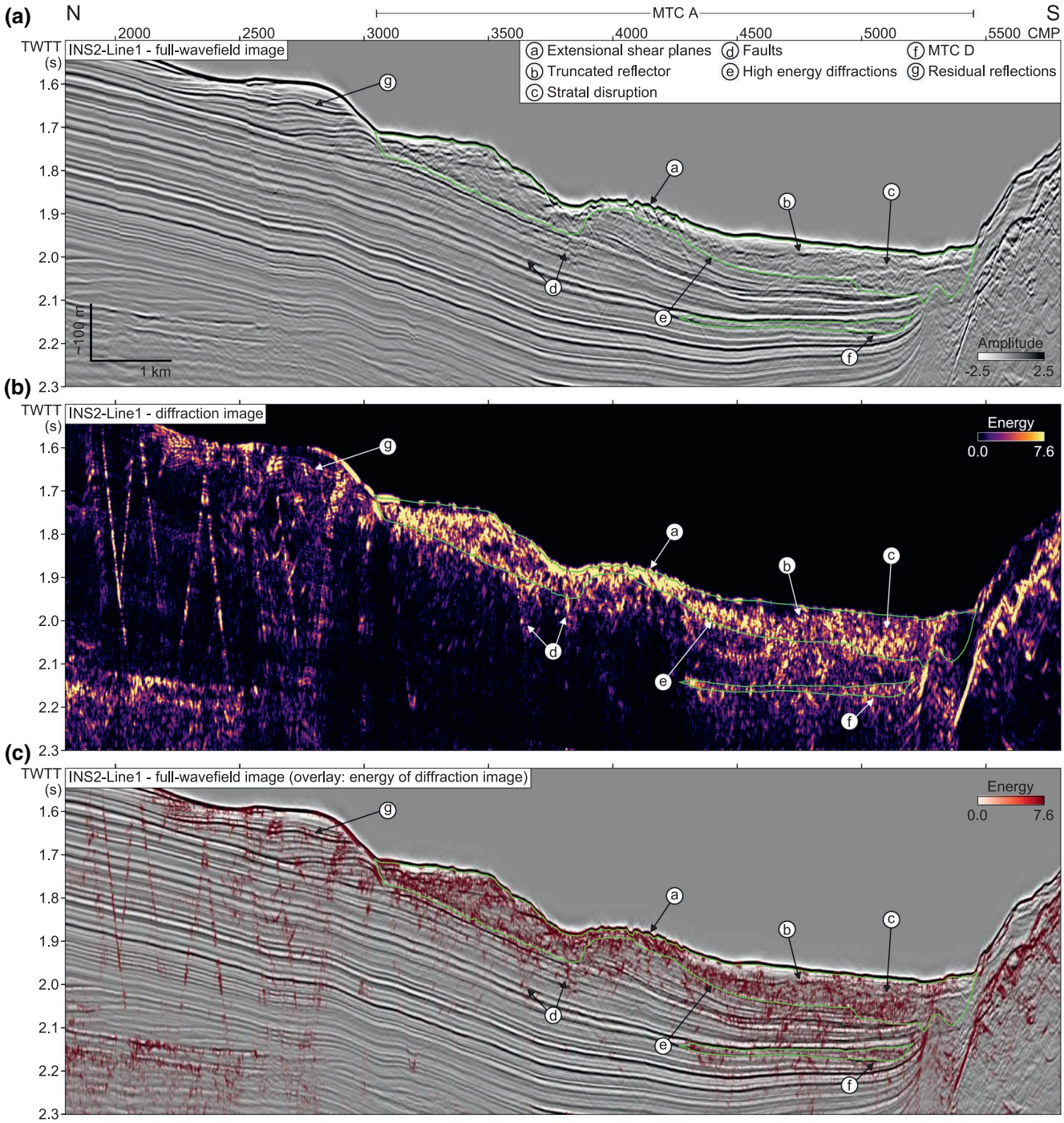

Figure 6. A section of seismic profile INS2-Line1 (Figure 5) from the Portimão Bank area containing a prominent mass-transport complex (MTC A). Speculative interpreted structure is labeled. (a) Full-wavefield seismic image, migrated reflections, and diffractions. (b) Diffraction image, migrated diffractions. (c) Energy of the diffraction image overlaid on the full-wavefield image, to highlight location of diffractors.

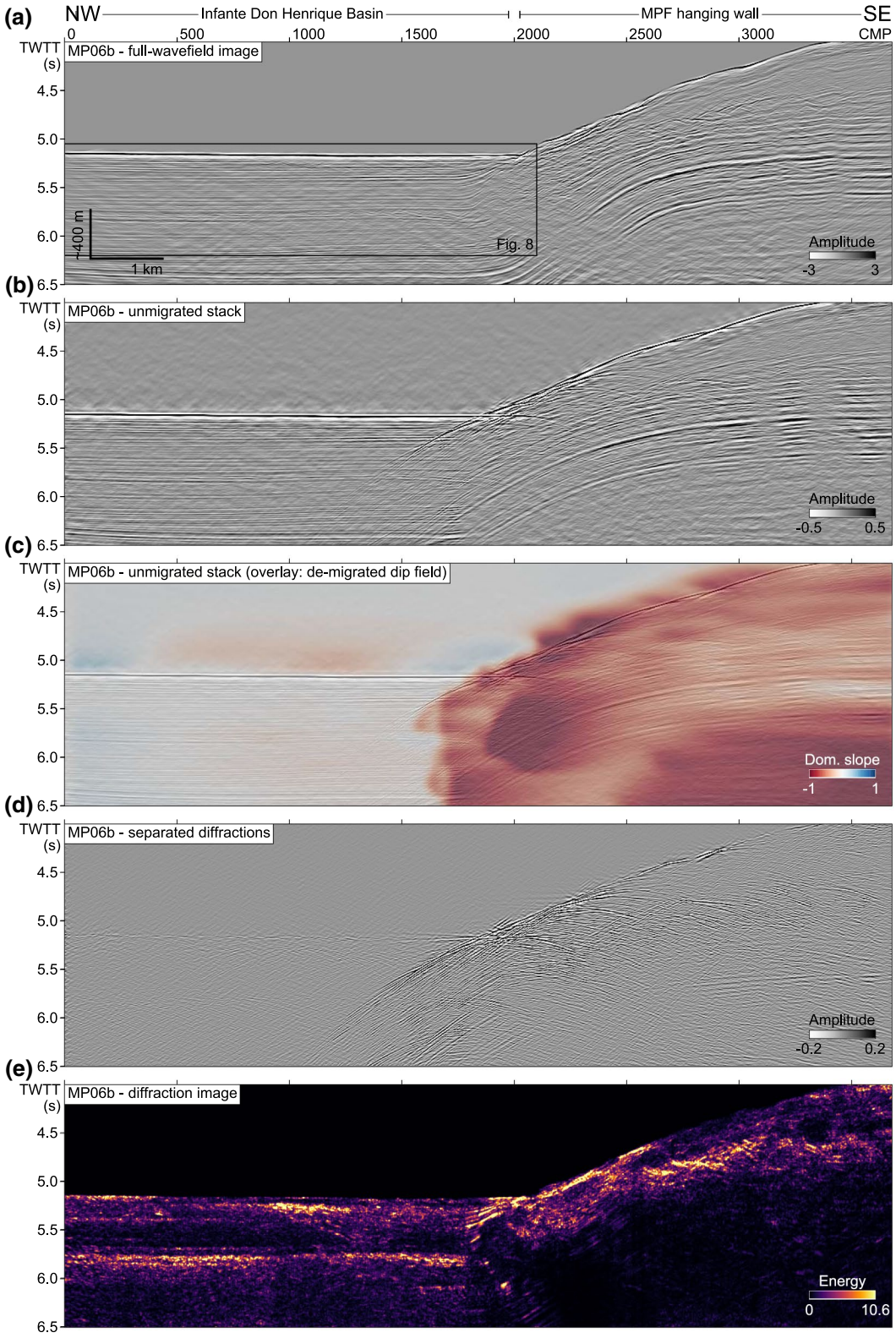

Figure 7. Seismic profile MP06b from the Marquês de Pombal fault zone area (Figure 2). The Marquês de Pombal fault (MPF) is located around CMP 2000. (a) Full-wavefield migrated seismic image. (b) Unmigrated stacked full-wavefield data. (c) Demigrated estimated dip field (dominant slope of reflectors) overlaid on the unmigrated full-wavefield stack. (d) Unmigrated stacked separated diffractions. (e) Diffraction image. CMP, common-midpoint.

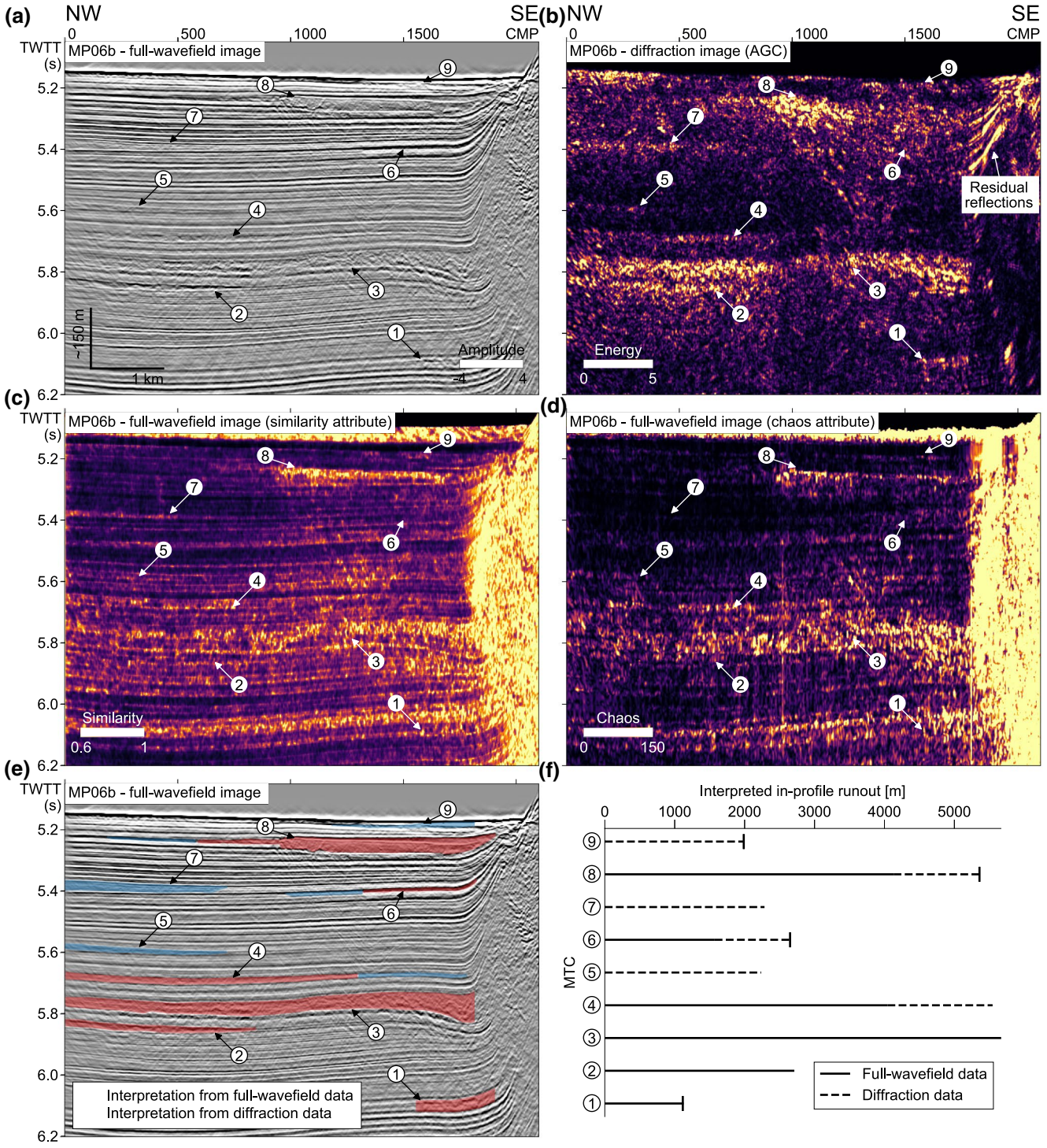

Figure 8. A section of seismic profile MP06b from the Marquês de Pombal fault area (Figure 7). Interpreted mass-transport complexes (MTCs) are labeled from 1 to 9. (a) Conventional full-wavefield seismic image. (b) Diffraction image. (c) The similarity attribute and (d) the chaos attribute derived from the full-wavefield seismic image. (e) The interpreted MTCs overlaid on the full-wavefield image. The extent of the bodies interpretable from the full-wavefield images and attributes is shaded red; the (extra) extent interpretable from the diffraction image is shaded blue. (f) The proportion of the apparent in-profile runout length of each body interpreted from the full-wavefield image and attributes, compared to that interpreted also using the diffraction image.

horizons well, showing near-zero slope in the Infante Don Henrique Basin and negative slope (i.e., dipping to the north west) in the hanging wall area. The south eastern, deep corner of the profile (CMPs > 2500, >5.5 s TWTT) shows anomalously high slope values corresponding to steeply dipping noise, due to the low signal-to-noise ratio in this part of the image. Figure 7d shows a stack of the separated diffractions, where diffraction tails are seen throughout, particularly from disrupted reflectors in the hanging wall area (CMPs 2000–4200) and corresponding to MTCs in the Infante Don Henrique Basin (CMPs 0–2000, 5.2–6 s TWTT). Figure 7e shows the diffraction image (i.e., the separated diffractions after migration), which contains laterally continuous, high-amplitude zones that correspond to MTCs seen in the full-wavefield seismic image. Some residual reflection energy remains, particularly in the area of rapidly varying dip at the break in slope corresponding to the Marquês de Pombal fault (CMP 2000, see Figure 8b).

4.2. Comparison of Full-Wavefield and Diffraction Images of Internal Structure

Figure 6 shows a section of seismic profile INS2-Line1 around MTC A, exposed at the seafloor (Figure 5), including the full-wavefield seismic image (Figure 6a), the corresponding diffraction image (Figure 6b) and the diffraction image overlaid on the full-wavefield image (Figure 6c). MTC A is characterized by a relatively high-amplitude response in the diffraction image, whereas the unfailed underlying sediments are characterized by a relatively low-amplitude response. This implies that MTC A contains a relatively high density of diffractors compared to the unfailed sediments. We speculate that these high-amplitude diffractions could result from (a) faults or shear planes in an extensional part of the MTC; (b) a truncated internal reflector within the MTC; (c) a zone of intense stratal disruption within the MTC (possibly the interface between two separate mass-transport deposits); (d) two small normal faults directly beneath the MTC, likely related to sediment loading/unloading after failure; (e) a zone of diffuse, high energy diffractors that is not clearly related to structure resolved by the full-wavefield image; and (f) a smaller, deeper MTC (MTC D). The remaining diffraction energy within the MTC has complex geometry and is not clearly related to structure resolved by the full-wavefield image (e.g., the area labeled “e”).

4.3. Comparison of Diffraction Image With Discontinuity Attributes

Figure 8 shows a section of seismic profile MP06b, focused on the stacked succession of MTCs in the Infante Don Henrique Basin. Figure 8a shows the full-wavefield seismic image, Figure 8c shows the similarity attribute of the full-wavefield image (similarity attribute implementation from OpendTect 6.4 with a time gate of 10 ms), and Figure 8d shows the chaos attribute of the full-wavefield image (“Chaotic Reflection” attribute implementation from Kingdom Rock Solid Attributes). Figure 8b shows the corresponding diffraction image. In general, the diffraction image appears to have lower noise and less interference from high-amplitude reflections than the discontinuity attributes of the full-wavefield image. There is a prominent zone of residual reflection energy at the break in slope across the Marquês de Pombal fault (labeled). In addition, a steeply dipping event cuts across part of the image from CMPs 800 to 1250, 5.2–5.6 s TWTT (seen also on the full-wavefield image and discontinuity attributes). We interpret this event as out-of-plane energy associated with MTC8, as it appears to originate from the edge of the thickest part of this body.

Interpretation of the MTCs is guided by one or more of the following features: (i) apparently chaotic or transparent seismic character in the full-wavefield seismic image; (ii) high-amplitude, laterally continuous top and/or basal bounding reflections; (iii) lobe shaped, laterally consistent low similarity/high chaos values; or (iv) lobe shaped, laterally consistent high-amplitude diffraction energy. In total, nine MTCs are interpreted from a combination of the full-wavefield image, derived attributes and the diffraction image (labeled in order of decreasing depth from MTC1 to MTC9). Three large bodies are directly visible in the full-wavefield seismic image (MTC3, MTC4, and MTC8). Two other bodies are only resolved by the diffraction image (MTC5 and MTC7). A further zone of high-amplitude diffractions close to the seafloor (CMPs 0–400, 5.15 s TWTT) is not interpreted as an MTC as the zone cuts across apparently parallel, undisturbed reflectors. We speculate that this diffraction energy could be from out-of-plane or generated by rough seafloor topography.

Figure 8e shows the interpreted lateral extent and thickness of the interpreted bodies overlaid on the full-wavefield seismic image. The portion of the bodies interpreted from the full-wavefield image and attributes

versus the diffraction image is indicated. Figure 8f shows the interpreted length (apparent in-profile runout) of these bodies, indicating the proportion of the total length interpretable only from the diffraction products. Several of the bodies (MTC2, MTC3, MTC4, MTC5, and MTC7) extend past the end of the section. In these cases the interpreted runout lengths are a lower bound on their total runout length in the direction of the profile. MTC4 and MTC6 are both resolved from the full-wavefield products, but by using the diffraction image their in-profile runout length is extended by >1.5 km and 1.1 km, respectively. MTC7 is only resolved by the diffraction image, likely because it has an apparently transparent seismic character in the full-wavefield seismic image, whereas the diffraction image clearly resolves a lobe shaped zone of heterogeneity. MTC9 is a 2-km long body near the seafloor that is only visible in the diffraction image, likely because it is thin enough to be masked in the full-wavefield seismic image by the relatively high-amplitude, long-wavelength seismic reflections.

4.4. Constraining the Location of Out-of-Plane Diffractors

4.4.1. Controlled Synthetic Demonstration

Figure 9 shows the results of the controlled synthetic demonstration of the "diffraction shadow" concept. This demonstration models an MTC body as a half-ellipsoid containing randomly placed point diffractors. Figure 9a shows the top and base boundaries of the body and the point diffractors (single-cell density anomalies). Figure 9b shows the forward modeled, zero-offset volume in time domain. As the model is composed entirely of diffractors (no reflections), this is equivalent to the ideal separated diffracted wavefield. Figure 9c shows the zero-offset volume after migration with a 3D constant velocity (v_p = 1,500 m s^{-1}) Stolt migration (Stolt, 1978), giving an idealized diffraction-only image. The diffractions are properly focused back to their apexes, which lie within the boundaries of the body (converted to TWTT). Some energy lies slightly outside these boundaries, due to the band-limited, zero-phase source wavelet. Figure 9d shows a single 2D section of the volume at y = 250 m, migrated with an equivalent 2D constant velocity Stolt migration. Out-of-plane diffracted energy is not properly imaged by the 2D migration. The result is a generally chaotic internal seismic character within the body (compare to Figure 9c) and a diffraction shadow that extends beneath the body with a maximum thickness of ~20 ms. The extent of the diffraction shadow agrees well with the predicted maximum extent based on the width of the body and Equation 1.

4.4.2. Real-Data Application

Figures 10a and 10b show the true basal surface of MTC A picked from the full-wavefield seismic image (INS2-Line1), alongside the picked base of the diffraction shadow, the limit of diffractions interpreted to be associated with MTC A. Figure 10c shows the lateral extent and thickness of MTC A, interpreted from a combination of multichannel seismic and subbottom profiler lines and the bathymetry, giving a total volume of 5.5 km^3 (converted from time to depth using the sediment velocity gradient of 200 m s^{-2}). The methodology, multichannel seismic profiles, and an example of one of the subbottom profiles are presented in the supplementary information (Text S2 and Figures S1–S4). Figure 10d shows the TWTT contour to the potential top surface of MTC A (the seafloor) from seismic profile INS2-Line1 (calculated using Equation 1), with the TWTT of the base diffraction shadow overlaid (magenta hatched area). This area shows the zone, perpendicular to the profile, of the potential locations of diffractors that could contribute to the diffraction shadow associated with MTC A. The half-width varies from a minimum of ~400 m to a maximum of ~900 m, implying that diffraction energy from at least 900 m from the vertical plane of the profile has contributed to the image.

5. Discussion

5.1. Imaging Internal Structure

The diffraction image for profile INS2-Line1 (Figure 6) clearly images a zone of normal faults between CMPs 1800 and 3000 and the rugose top salt interface of the Lolita salt diapir—both classic targets for diffraction imaging. The zone of normal faults, in particular, appears significantly better resolved compared to the full-wavefield image, where their small offset means they are barely visible. There is also a significantly higher concentration of diffraction energy within MTC A compared to the surrounding unfailed sediments.

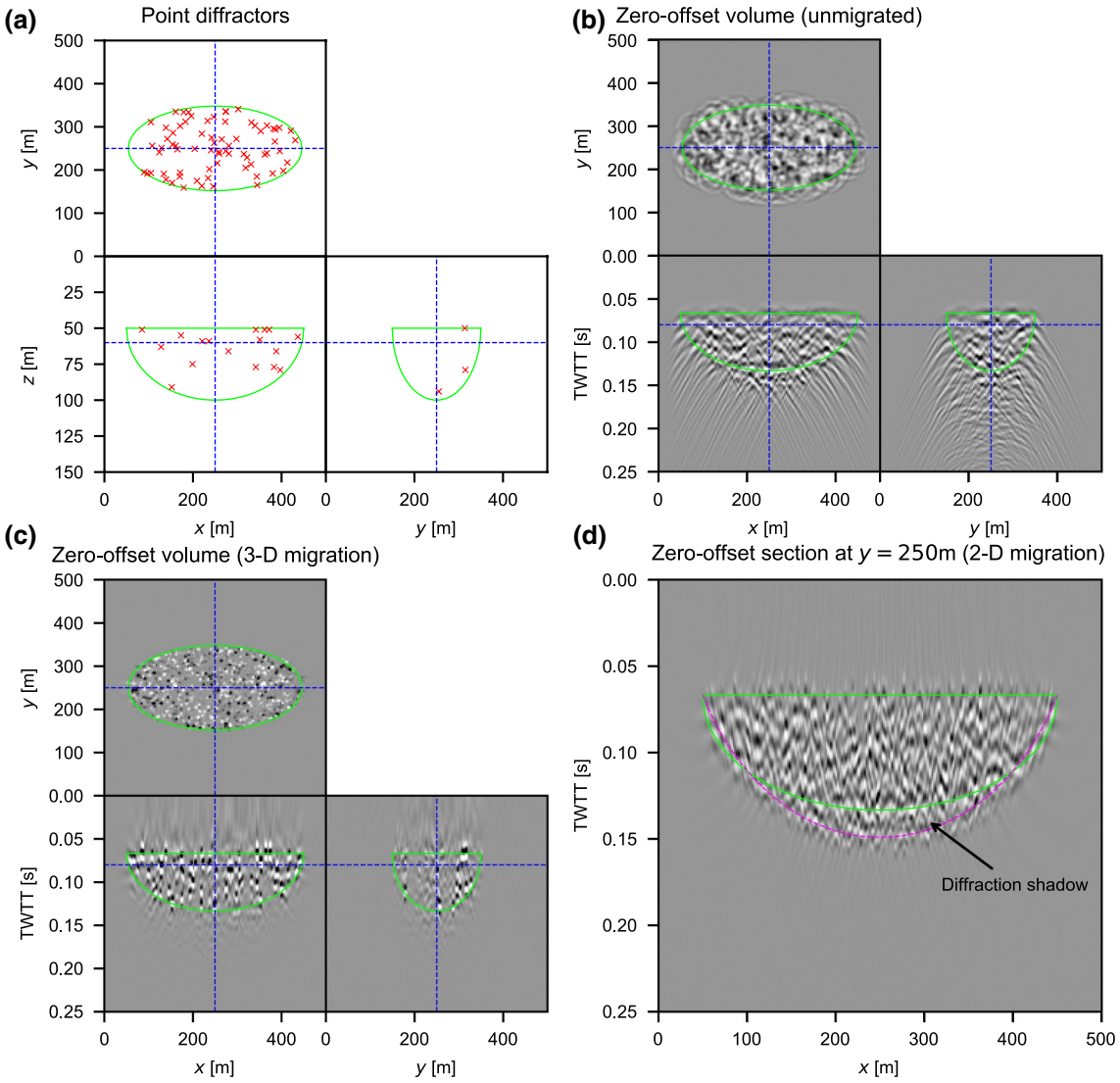

Figure 9. Controlled synthetic demonstration model setup and results. The boundaries of the half-ellipsoidal zone representing a mass-transport complex (MTC) are outlined in green. (a) 3D model definition showing location of point diffractors (single-cell density anomalies) randomly placed within the MTC zone. (b) 3D forward modeled zero-offset volume. (c) 3D Stolt migration of (b). (d) 2D Stolt migration of a 2D slice of (b) at $y = 250$. The base of the diffraction shadow predicted by Equation 1 is shown in dashed magenta.

This suggests that the internal structure of MTC A contains significantly more wavelength and subwavelength-scale discontinuities compared to the unfailed sediments, which can already be seen from the full-wavefield seismic image. This is consistent with outcrop examples of MTCs, which show that complex meter-scale internal structure can be preserved (Lucente & Pini, 2003). We observe high-amplitude diffractors that coincide with structure observed on the reflection image related to MTC A: headscarp faults, truncated internal interfaces, and strong stratal disruption. This is the type of small-scale (i.e., potentially subwavelength) geological heterogeneity that we would expect to generate diffractions (Figure 1).

Diffractors that do not coincide with structure seen in the full-wavefield seismic image are also resolved (labeled "e" in Figure 6). In the absence of high-resolution data, such as cores or subbottom profiler images, it is not clear exactly what type of structure these diffractors represent; we speculate that they may be related to small-scale internal structure that is also not well imaged by the full-wavefield image, such as local shear zones, intact embedded blocks or fluid escape features. Diffractions require both lateral heterogeneity (around or below the scale of the seismic wavelength) *and* an impedance contrast, so the presence

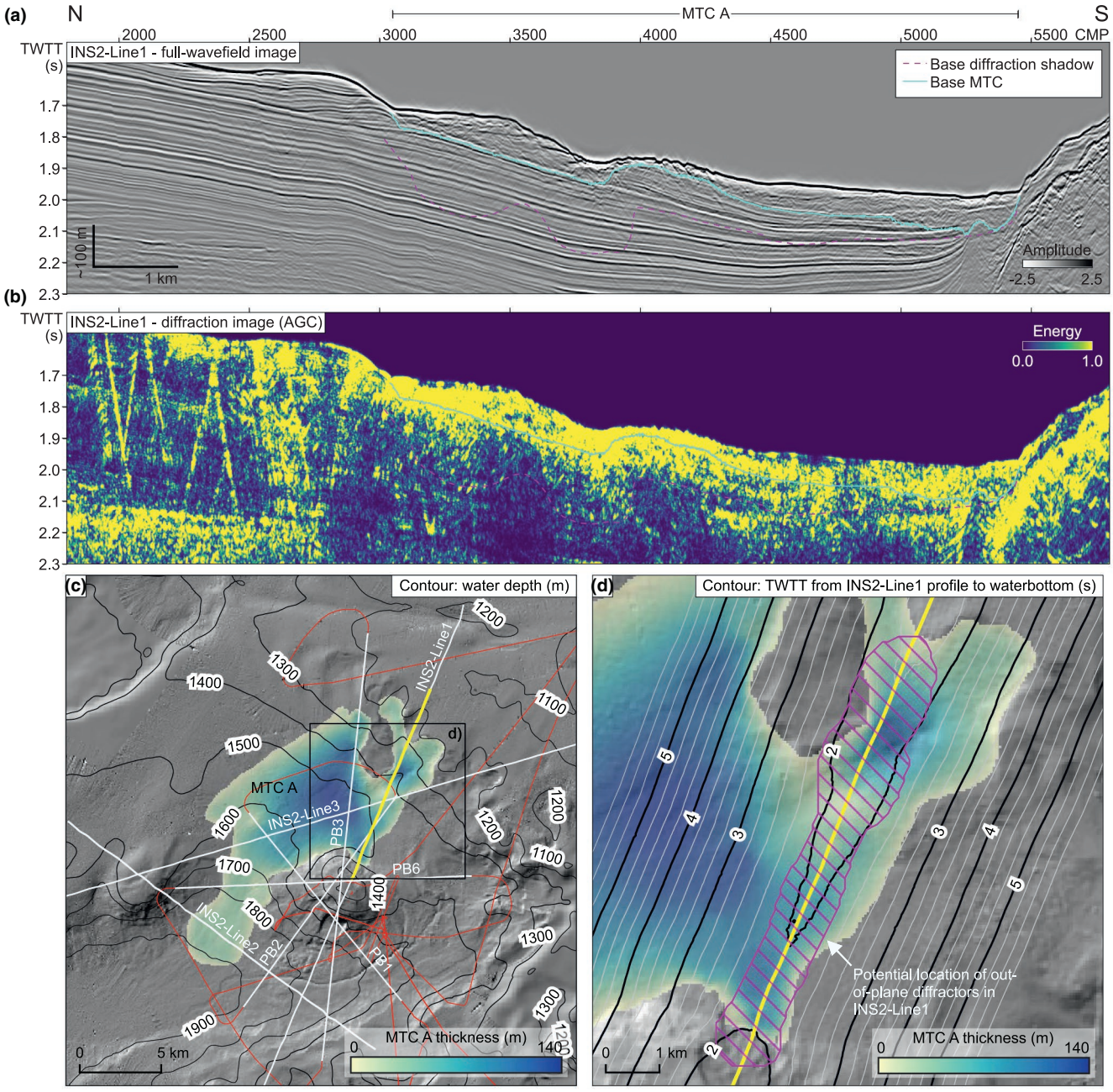

Figure 10. A section of seismic profile INS2-Line1 (Figure 5) containing MTC A. (a) The full-wavefield seismic image. (b) The corresponding diffraction image, with interpreted basal surface from the full-wavefield image (solid blue) and interpreted base of the out-of-plane diffractions associated with MTC A (the diffraction shadow, dashed magenta). (c) Water depth (contours) on the shaded relief of the area surrounding the Lolita salt diapir. The extent and thickness of MTC A is interpreted from the bathymetry, subbottom profiler data (red) and a network of multichannel seismic profiles (white). (d) Contour lines show the two-way travel time (TWTT) calculated from seismic datum to the seafloor (potential top MTC A surface) at each CMP location, perpendicular to the profile (Section 3.4.2). The hatched magenta area indicates the zone of potential locations for the out-of-plane diffractors implied by the base diffraction shadow pick in (a) and (b). MTC, mass-transport complex; CMP, common-midpoint.

of diffractions within a body is evidence that significant wavelength-scale (i.e., meter to decameter) internal structure is preserved after transport or generated during emplacement. Diffraction images can thus provide information on the degree of internal disaggregation or organization by quantifying the degree of geological heterogeneity at scales close to the seismic resolution. High diffraction density within an MTC is likely to be associated with relatively low disaggregation, as it implies that wavelength-scale internal structure is preserved. Conversely, low diffraction density within an MTC could imply significant disaggregation—the scale of internal structure has been reduced to much lower than the seismic wavelength by mass-movement processes. The magnitude of the diffraction energy could therefore provide an extra source of information to constrain flow type, for example, to differentiate between debris flows (complete disaggregation and destruction of prefailure internal interfaces), slumps (prefailure internal interfaces deformed but largely preserved), and the transition between both end members. The high-amplitude diffraction image response observed in Figure 6b supports an interpretation of MTC A as a "structured" rather than "structureless" deposit, even if the geometry of such structure is not well resolved by the seismic profiles used in this study.

We also resolve two normal fault planes *below* MTC A in the diffraction image (labeled "d" in Figure 6). One is associated with a ~500-m wide, channel-shaped depression on the top surface of MTC A around CMP 3750. We interpret these faults to be the result of sediment loading due to the emplacement of MTC A on the previously competent sediments, as the faults become blind at depth. As well as resolving structure within MTCs, diffraction imaging is able to image small-scale, discontinuous structure in the unfailed sediments immediately *below* the basal shear surface.

5.2. Discrimination of Events Near the Limit of Seismic Resolution

The Infante Don Henrique basin hosts a >1-s TWTT thick succession of stacked MTCs (Figure 8). Some large events in profile MP06b ($n = 6$) are clearly visible on the full-wavefield seismic image as apparently chaotic bodies with well-defined top and basal reflectors. The diffraction image, however, reveals several smaller events ($n = 3$) that are difficult to identify or are ambiguous in the full-wavefield seismic image and associated discontinuity attributes. We interpret these events as MTCs, because they are associated with high-amplitude reflectors (characteristic of the top and basal surfaces) and their diffraction response has relatively sharp boundaries, indicating that they are not, for example, more extensive regional erosive unconformities. Nonetheless, it is important to remember that diffraction images only identify small-scale heterogeneous geology—they are not directly diagnostic for MTCs. Features with a similar diffraction response could include slightly erosional (e.g., furrowed) surfaces, such as those associated with turbidity currents.

In addition, the diffraction image allows for better definition of the apparent lateral extent (runout) of bodies. We are able to follow the apparent in-profile runout of some events for significant extra distance (on the order of kilometers for seismic profile MP06b) compared to the full-wavefield seismic image (Figure 8f). We also observe this effect on seismic profile INS2-Line1 (Figure 6) where there is a small MTC (MTC D, labeled "f" in Figure 6) below the larger event, MTC A. In the full-wavefield seismic image, MTC D is represented by a short (less than 500 m), high-amplitude basal horizon. The diffraction image shows a lobe shaped zone of heterogeneity, ~3 km in length, that we interpret as a small MTC that failed toward the north, originating from the dome associated with the Lolita salt diapir.

Diffraction images in general offer higher lateral (i.e., horizontal) resolution because they overcome the lateral resolution limit of seismic reflections. In the context of screening for MTCs, diffraction images also improve the discrimination of relatively small, thin events (on the order of 10 ms TWTT thick, Figure 8). This improvement is a result of removing the relatively high-amplitude reflections, which can mask thin zones of discontinuous geology. In the MP06b profile, the unfailed confining sediments have a seismic character dominated by high-amplitude, long-wavelength reflections that are parallel to the MTCs. In addition, the MTCs themselves generate strong reflections at their top and basal surfaces. The apparent vertical thickness of these reflections is related to the dominant wavelength of the seismic source and is independent of the true thickness of the body. This means that the relatively high-amplitude and long-wavelength reflections can obscure thin, discontinuous geobodies that may otherwise be properly imaged by full-wavefield seismic imaging. By eliminating these masking reflections, the effective *interpretable* vertical resolution is increased for discontinuous, diffraction generating bodies that are thinner than the dominant seismic wavelength.

Consequently, diffraction images allow more accurate delineation of the total lateral extent of MTCs when a significant proportion of the body is thinner than the reflection image can resolve. This is particularly important to characterize the flow properties of unconfined mass-movements from seismic data. Many events have a substantial component of fine sediment that runs out a significant distance beyond the main cohesive body of the event, pinching out at zero thickness at the true maximum extent of the flow. This type of thin deposit, parallel to the background sedimentation, is difficult to image with full-wavefield seismic images for the reasons outlined above.

The record of buried MTCs identified from marine geophysical data is biased toward events that can be clearly resolved in multichannel seismic reflection images (i.e., relatively thick and laterally extensive). This means that catalogs of MTCs are biased toward larger events or younger events that are still preserved in the bathymetry (Urgeles & Camerlenghi, 2013). Screening for MTCs using diffraction imaging will allow for a more complete catalog of smaller, deeper events, with more confident estimation of their true total runout.

5.3. Comparison to Seismic Discontinuity Attributes

Seismic discontinuity attributes are routinely computed as part of a traditional geohazard interpretation workflow in order to screen for, characterize, and delineate MTCs (e.g., Alves et al., 2014; Bhatnagar et al., 2019). Here, we calculate the similarity and chaos attributes of the full-wavefield seismic image to compare to the diffraction image (Figure 8). There are high-level similarities: areas with low similarity and high chaos values tend to correspond to areas of high diffraction energy. Relatively large events (MTC3, MTC4, and MTC8) are clearly imaged by both attributes and by the diffraction image. Several smaller events, however, are not clearly delineated from the background geology by the discontinuity attributes. Moreover, both the chaos and similarity attribute seem to be sensitive to features other than geological discontinuities—we observe low similarity, high chaos values for high-amplitude, laterally continuous horizons (i.e., reflections) in the unfailed sediments that host the MTCs. It is difficult to discriminate a high-amplitude, horizontal unfailed horizon from a thin MTC using these discontinuity attributes.

Preine et al. (2020) suggest that diffraction images may be a more "physically correct" alternative to using traditional discontinuity attributes to support interpretation of faults and fractures. We argue that this is also the case for interpretation of MTCs, because diffraction images are directly sensitive to the target geology (i.e., bodies likely to contain wavelength and subwavelength-scale discontinuities); eliminate relatively high-amplitude, long-wavelength coherent reflections (which can interfere with attributes and mask thin bodies); and do not suffer from edge effects and smoothing that may be introduced by window-based attributes.

5.4. Constraining the Lateral Extent of MTCs From 2D Profiles

Seismic imaging in 2D assumes that the recorded energy is reflected or diffracted from the 2D vertical plane along the seismic profile. This may be a reasonable assumption where geological structure is 1D perpendicular to the plane of the profile (a so-called dip line). When reflectors dip obliquely with respect to the profile, reflections cannot be properly imaged with a 2D migration. Energy reflected from out-of-plane is not properly located in TWTT and may interfere with primary in-plane energy. MTCs are inherently 3D geobodies—in addition to internal structure, they often show rugose, nonconformal upper and basal surfaces and steep, erosive lateral margins that can generate high-amplitude reflections and diffractions (Figure 1). This means that there is rarely an optimal direction to acquire a well-imaged 2D seismic "dip line" across an MTC. In other words, out-of-plane energy is a common feature of 2D seismic images of MTCs. The superior illumination of diffractions means that diffraction images will contain proportionally more out-of-plane energy than full-wavefield images.

Figure 9 demonstrates this effect with a controlled synthetic test, where an MTC body is simulated as a half-ellipsoidal zone of point diffractors. The results show that while 3D migration is properly able to image and locate diffractors in space, a 2D seismic acquisition and image will inevitably contain a large proportion of out-of-plane diffractions. The 2D migrated section shows an apparently "chaotic" texture, despite there being no chaotic reflectors inside the MTC (Figure 9d). We speculate that out-of-plane diffractions could be partly responsible for the commonly observed apparently chaotic internal seismic response of MTCs in

2D seismic profiles. This result underlines the importance of acquiring 3D seismic data for good imaging and proper reconstruction of the geometry of the internal structure of MTCs, both for conventional full-wavefield seismic imaging and for diffraction imaging.

In Section 3.4, we propose a simple workflow to constrain the original location of out-of-plane diffracted energy imaged in a 2D seismic profile. Under certain (strong) assumptions, the results can be used to estimate a minimum bound on the lateral extent, perpendicular to the profile, of the zone of diffractors that contribute to the diffraction image—a constraint on the minimum half-width of an MTC imaged by a 2D seismic profile. The controlled synthetic test shows that Equation 1 can predict the apparent thickness of this diffraction shadow (Figure 9d). We also demonstrate the method on a real-data example by applying it to profile INS2-Line1, where there is a visible diffraction shadow beneath MTC A (Figure 10). The presence of diffractions associated with MTC A, but beneath its apparent basal surface, indicates that the diffraction image contains energy from outside the plane of the profile. Does this real-data example satisfy the assumptions stated in Section 3.4? It seems reasonable to assume that this MTC does contain diffractors spread throughout the body, as we consistently see an elevated response in the diffraction image throughout the 2D profile in a downslope direction (Figure 6). The maximum TWTT thickness of MTC A is ~150 ms at a depth of ~1.7 s TWTT, therefore we can consider this MTC to be a "thin body." MTC A is exposed at the seafloor, so we can be confident that the overburden velocity is constant (water velocity) and laterally homogeneous perpendicular to the profile. The remaining assumption is that there exists a well-defined diffraction shadow associated with the body. In the lower part of the body, the diffraction shadow appears to be associated with MTC A, as in the controlled synthetic test. In the upper part of the body, however, there is significant uncertainty around whether the interpreted diffractors are associated with the MTC. For this real-data example, the resulting zone of potential diffractors has half-width comparable to or lower than the distance to the edge of MTC A in the direction of maximum extent (Figure 10d). This indicates that perhaps this zone of potential diffractors could be a realistic lower bound on the width of the MTC with respect to the seismic profile. On the other hand, interpreting the base of the diffraction shadow will always be the part of this workflow that introduces the greatest uncertainty. Even though this is a crude technique, with large errors, it is still an informative exercise to think about where these out-of-plane diffractors could come from, and how this relates to the overall geometry of an imaged MTC.

The method proposed in Section 3.4 is simple but nevertheless could be a useful way to estimate a lower bound on the extent of an MTC from a single 2D seismic profile, where other geophysical information is not available. This is a common scenario when screening for MTCs for marine geohazard studies in frontier areas; for academic and vintage datasets; and in polar areas, where acquiring 3D towed-streamer seismic data may be impossible due to year-round ice cover. It is trivial to extend the method to deal with buried MTCs, so long as (i) the velocity model to the top of the body is known; (ii) the slide is thin relative to its depth; and (iii) the topography of the top surface is small, relative to its depth. Future studies should validate this approach for a realistic scenario by repeating the workflow for the controlled synthetic test with a 2D profile extracted from a real-data 3D volume.

5.5. Limitations of Diffraction Imaging to Characterize MTCs

While we have shown that diffraction images offer better imaging of small-scale discontinuous geology compared to reflection images, there remain some limitations, particularly regarding the data used for this study and the specific application to characterize MTCs.

5.5.1. Incomplete Diffraction Separation

Diffraction imaging relies on good separation between the diffracted and reflected wavefields. Here, we perform the diffraction separation in common-offset domain using PWD filters to eliminate laterally continuous reflections. Subaqueous mass-failures tend to occur in environments that are geologically complex, such as canyons, tectonically active areas and diapiric areas. In such environments, seismic images are likely to contain strong variation in dip, reflections that are not laterally continuous and high-amplitude reflections and diffraction tails generated by a rugose seafloor. These factors can prevent reliable estimation of the true dip field from unmigrated seismic profiles. Our solution is to estimate the dip field on migrated data and demigrate the dip field for diffraction separation on the unmigrated common-offset sections. In

general, the results of the dip estimation and demigration are adequate for diffraction separation to image the shallow MTCs in this study. There are, however, some residual reflections that are not eliminated during diffraction separation, contaminating the diffraction images (Section 4.1). In practice, these can often be identified by carefully comparing the full-wavefield and diffraction images, as residual reflections will migrate to the same location and TWTT in both.

Other diffraction separation methods may be better suited to imaging MTCs in geologically complex settings. These include postmigration diffraction separation in dip-angle domain (Reshef & Landa, 2009) and diffraction separation by adaptive subtraction of the coherent reflected wavefield (Schwarz, 2019a). The choice of method ultimately depends on the seismic acquisition (e.g., streamer length compared to target depth, lateral and vertical image resolution, 2D vs. 3D acquisition geometry), data characteristics (e.g., amplitude of diffractions relative to reflections, signal-to-noise level), and confidence in the velocity model. In all cases, the preprocessing flow must be designed to preserve diffraction energy.

5.5.2. Migration Velocities

For the seismic profiles analyzed in this study, migration velocity analysis by focusing diffractions or moveout analysis of reflections was not possible (Section 3.3). The data were acquired using a short streamer relative to the water depth, so there is no significant differential moveout of reflection events in CMP domain to perform a robust semblance-based velocity analysis. We found that the separated diffracted wavefield was routinely contaminated with out-of-plane diffractions, which would focus diffractions at an incorrect velocity and at an incorrect TWTT. Instead, we use migration velocities derived from simple velocity gradients in the shallow sediments, as the target MTCs are shallow with respect to the water depth. A test of the sensitivity of diffraction imaging to the chosen migration velocity is presented in the supplementary information (Figure S7).

Future studies should concentrate on mitigating the effect of out-of-plane diffractions for focusing migration velocity analysis from 2D seismic profiles (e.g., Preine et al., 2020). This could be achieved by weighting the focusing analysis toward continuous diffraction generating structures such as faults, or deeper diffractors that are less biased by not being exactly in-plane. The problem of out-of-plane diffractions is resolved with 3D seismic data, because 3D migrations can collapse diffractions to their true apex.

6. Conclusions

In this study, we use two 2D marine multichannel seismic profiles from the Gulf of Cadiz (south west Iberian Margin) to compare the ability of seismic diffraction imaging to conventional full-wavefield seismic imaging to characterize MTCs. Diffraction images can be considered to primarily image small-scale, discontinuous geological structure and have higher lateral resolution compared to full-wavefield seismic images. We find that in these examples MTCs generate a large contribution of diffracted energy compared to the surrounding unfailed confining sediments, likely because the scale of their internal structure and rugose erosional basal surface is close to, or below, the scale of the seismic wavelength.

Our results suggest that diffraction imaging can

1. image internal structure of MTCs that is not well resolved by full-wavefield seismic images;
2. be used to better estimate the full extent of MTCs which have thin runout and to identify small events that are close to the resolution of the full-wavefield seismic image;
3. be a constraint on the overall scale of internal heterogeneity, important to classify flow type for MTCs that show an apparently chaotic or transparent seismic response; and
4. be considered as a more physically justified alternative to traditional seismic discontinuity attributes to support interpretation of MTCs.

In addition, we show that 2D diffraction images of MTCs are likely to include significant contributions of misplaced out-of-plane diffracted energy, due to the inherent 3D nature of MTCs. We suggest that, under certain strong assumptions, this energy (usually considered noise) may be used to constrain the 3D geometry of MTCs from single 2D seismic profiles by providing a minimum bound on the cross-line width. We demonstrate this using a controlled synthetic test and on one of the real-data profiles.

Characterization of MTCs and their internal structure is a promising new application of diffraction imaging, potentially bridging the "resolution gap" between seismic data and outcrop studies. Our results underline the importance of preserving diffractions through the processing flow for lateral resolution (including for full-wavefield seismic images) and the importance of 3D seismic imaging to properly characterize complex geology such as MTCs. Better imaging provides important constraints on the failure and emplacement dynamics of MTCs, crucial for improving our understanding of the geohazard posed by subaqueous mass-movements.

Appendix A: Dip Demigration

The aim of dip demigration is to recover the unmigrated dip field from a dip field estimated on a migrated image. We use this technique due to the presence of high-amplitude, steeply dipping diffraction tails and poor reflector continuity throughout the unmigrated data used in this study.

We perform the dip demigration using simple geometric relations that describe how migration affects dipping reflectors in 2D (Yilmaz, 2001):

1. The dip in a migrated section is greater than in the unmigrated section (migration *steepens* reflectors).
2. For areas of nonzero local dip, the horizontal distance between points is shorter after migration.
3. Migration moves events in an updip direction.

After Chun and Jacewitz (1981), for migrated dip α', unmigrated dip α, local migration velocity, v, and TWTT t:

$$\begin{aligned} \alpha' &= \frac{\alpha}{\sqrt{1-(\frac{\alpha v(x,t)}{2})^2}} \\ x' &= \frac{v(x,t)^2 t}{4}\alpha \\ t' &= t\left(1-\sqrt{1-\frac{\alpha v(x,t)}{2}}\right). \end{aligned} \tag{A1}$$

We first solve for the unmigrated local dip value, $\alpha(x', t')$. Then, we calculate the horizontal and vertical (time) shift ($x'-x$ and $t'-t$). The demigrated dip field $\alpha(x, t)$ is estimated by applying image warping (with the horizontal and vertical shifts) to $\alpha(x', t')$. The effect is to reverse the effect of migration on the dip field, to "demigrate" the dip field.

Acknowledgments
The authors wish to thank the crew, technicians, and scientific party of the INSIGHT cruises (Legs 1 and 2), particularly the onboard seismic processing team: R. Bartolomé, P. Brito, A. Calahorrano, and E. Piazza. We are grateful to J. Preine, an anonymous reviewer, and the associate editor for thoughtful and constructive reviews which significantly improved the quality of this article. Data for this study were collected in the framework of the project INSIGHT (CTM2015-70155-R) funded by the Spanish "Ministerio de Ciencia e Innovación" and the European Regional Development Fund. J. Ford was supported by a Marie Curie Doctoral Fellowship through the SLATE Innovative Training Network within the European Union Framework Program for Research and Innovation Horizon 2020 under grant agreement no. 721403.

Data Availability Statement

Preprocessed prestack seismic data, processing horizons, migration velocities, and code to reproduce the results using Madagascar (Fomel et al., 2013) are archived in Ford (2020).

References

Alsop, G. I., & Marco, S. (2013). Seismogenic slump folds formed by gravity-driven tectonics down a negligible subaqueous slope. *Tectonophysics*, *605*(48–69), 48–69. https://doi.org/10.1016/j.tecto.2013.04.004

Alves, T. M., Kurtev, K., Moore, G. F., & Strasser, M. (2014). Assessing the internal character, reservoir potential, and seal competence of mass-transport deposits using seismic texture: A geophysical and petrophysical approach. *AAPG Bulletin*, *98*(4), 793–824. https://doi.org/10.1306/09121313117

Badhani, S., Cattaneo, A., Collico, S., Urgeles, R., Dennielou, B., Leroux, E., et al. (2020). Integrated geophysical, sedimentological and geotechnical investigation of submarine landslides in the Gulf of Lions (Western Mediterranean). *Geological Society, London, Special Publications*, *500*(1), 359–376. https://doi.org/10.1144/SP500-2019-175

Baptista, M., Heitor, S., Miranda, J., Miranda, P., & Victor, L. (1998). The 1755 Lisbon tsunami; evaluation of the tsunami parameters. *Journal of Geodynamics*, *25*(1–2), 143–157. https://doi.org/10.1016/S0264-3707(97)00019-7

Baptista, M., & Miranda, J. (2009). Revision of the Portuguese catalog of tsunamis. *Natural Hazards and Earth System Sciences*, *9*(1), 25–42. https://doi.org/10.5194/nhess-9-25-2009

Berndt, C., Costa, S., Canals, M., Camerlenghi, A., de Mol, B., & Saunders, M. (2012). Repeated slope failure linked to fluid migration: The Ana submarine landslide complex, Eivissa Channel, Western Mediterranean Sea. *Earth and Planetary Science Letters*, *319–320*, 65–74. https://doi.org/10.1016/j.epsl.2011.11.045

Bhatnagar, P., Verma, S., & Bianco, R. (2019). Characterization of mass transport deposits using seismic attributes: Upper Leonard Formation, Permian Basin. *Interpretation*, *7*(4), SK19–SK32. https://doi.org/10.1190/INT-2019-0036.1

Born, M., & Wolf, E. (1959). *Principles of optics: Electromagnetic theory of propagation, interference, and diffraction of light*. London: Pergamon Press.

Brackenridge, R. E., Hernández-Molina, F. J., Stow, D. A. V., & Llave, E. (2013). A Pliocene mixed contourite–turbidite system offshore the Algarve Margin, Gulf of Cadiz: Seismic response, margin evolution and reservoir implications. *Marine and Petroleum Geology*, *46*, 36–50. https://doi.org/10.1016/j.marpetgeo.2013.05.015

Bull, S., Cartwright, J., & Huuse, M. (2009). A review of kinematic indicators from mass-transport complexes using 3D seismic data. *Marine and Petroleum Geology*, *26*(7), 1132–1151. https://doi.org/10.1016/j.marpetgeo.2008.09.011

Bull, S., & Cartwright, J. A. (2020). Line length balancing to evaluate multi-phase submarine landslide development: An example from the Storegga Slide, Norway. *Geological Society, London, Special Publications*, *500*(1), 531–549. https://doi.org/10.1144/SP500-2019-168

Cardona, S., Wood, L. J., Day-Stirrat, R. J., & Moscardelli, L. (2016). Fabric development and pore-throat reduction in a mass-transport deposit in the Jubilee Gas Field, Eastern Gulf of Mexico: Consequences for the sealing capacity of MTDs. In G. Lamarche, J. Mountjoy, S. Bull, T. Hubble, S. Krastel, E. Lane, et al. (Eds.), Submarine mass movements and their consequences (Vol. 41, pp. 27–37). Cham, Switzerland: Springer. https://doi.org/10.1007/978-3-319-20979-1_3

Carter, L., Gavey, R., Talling, P., & Liu, J. (2014). Insights into submarine geohazards from breaks in subsea telecommunication cables. *Oceanography*, *27*(2), 58–67. https://doi.org/10.5670/oceanog.2014.40

Chen, J., & Schuster, G. T. (1999). Resolution limits of migrated images. *Geophysics*, *64*(4), 1046–1053. https://doi.org/10.1190/1.1444612

Chopra, S., & Marfurt, K. J. (2007). *Seismic attributes for prospect identification and reservoir characterization*. Tulsa, OK: Society of Exploration Geophysicists. https://doi.org/10.1190/1.9781560801900

Chun, J. H., & Jacewitz, C. A. (1981). Fundamentals of frequency domain migration. *Geophysics*, *46*(5), 717–733. https://doi.org/10.1190/1.1441211

Claerbout, J. F. (1992). *Earth soundings analysis: Processing versus inversion*. London: Blackwell Scientific Publications.

Decker, L., Janson, X., & Fomel, S. (2015). Carbonate reservoir characterization using seismic diffraction imaging. *Interpretation*, *3*(1), SF21–SF30. https://doi.org/10.1190/INT-2014-0081.1

Decker, L., Merzlikin, D., & Fomel, S. (2017). Diffraction imaging and time-migration velocity analysis using oriented velocity continuation. *Geophysics*, *82*(2), U25–U35. https://doi.org/10.1190/geo2016-0141.1

Dell, S., & Gajewski, D. (2011). Common-reflection-surface-based workflow for diffraction imaging. *Geophysics*, *76*(5), S187–S195. https://doi.org/10.1190/geo2010-0229.1

Diviacco, P., Rebesco, M., & Camerlenghi, A. (2006). Late Pliocene mega debris flow deposit and related fluid escapes identified on the Antarctic peninsula continental margin by seismic reflection data analysis. *Marine Geophysical Researches*, *27*(2), 109–128. https://doi.org/10.1007/s11001-005-3136-8

Fomel, S. (2002). Applications of plane-wave destruction filters. *Geophysics*, *67*(6), 1946–1960. https://doi.org/10.1190/1.1527095

Fomel, S., Landa, E., & Taner, M. (2007). Poststack velocity analysis by separation and imaging of seismic diffractions. *Geophysics*, *72*(6), U89–U94. https://doi.org/10.1190/1.2781533

Fomel, S., Sava, P., Vlad, I., Liu, Y., & Bashkardin, V. (2013). Madagascar: Open-source software project for multidimensional data analysis and reproducible computational experiments. *Journal of Open Research Software*, *1*(1), e8. https://doi.org/10.5334/jors.ag

Ford, J. (2020). Multi-channel seismic reflection profiles MP06b and INS2-Line1 (INSIGHT cruises). Zenodo (Data set). https://doi.org/10.5281/zenodo.3946170

Frey Martinez, J., Cartwright, J., & Hall, B. (2005). 3D seismic interpretation of slump complexes: Examples from the continental margin of Israel. *Basin Research*, *17*(1), 83–108. https://doi.org/10.1111/j.1365-2117.2005.00255.x

Gafeira, J., Long, D., Scrutton, R., & Evans, D. (2010). 3D seismic evidence of internal structure within Tampen Slide deposits on the North Sea Fan: Are chaotic deposits that chaotic? *Journal of the Geological Society*, *167*(3), 605–616. https://doi.org/10.1144/0016-76492009-047

Gazdag, J., & Sguazzero, P. (1984). Migration of seismic data by phase shift plus interpolation. *Geophysics*, *49*(2), 124–131. https://doi.org/10.1190/1.1441643

Gràcia, E., Dañobeitia, J., Vergés, J., Bartolomé, R., & Córdoba, D. (2003). Crustal architecture and tectonic evolution of the Gulf of Cadiz (SW Iberian margin) at the convergence of the Eurasian and African plates. *Tectonics*, *22*(4), 1033. https://doi.org/10.1029/2001TC901045

Gràcia, E., Dañobeitia, J., Vergés, J., & PARSIFAL Team. (2003). Mapping active faults offshore Portugal (36°N–38°N): Implications for seismic hazard assessment along the southwest Iberian margin. *Geology*, *31*(1), 83. https://doi.org/10.1130/0091-7613(2003)031⟨0083:MAFOPN⟩2.0.CO;2

Gràcia, E., Urgeles, R., Rothenbeck, M., Wenzlaff, E., Steinführer, A., Kurbjuhn, T., et al. (2018). ImagiNg large SeismogenIc and tsunamiGenic structures of the Gulf of Cadiz with ultra-High resolution Technologies (INSIGHT) Leg 1 survey cruise report (Tech. Rep.). Barcelona: Institute of Marine Sciences.

Gràcia, E., Vizcaino, A., Escutia, C., Asioli, A., Rodés, Á., Pallàs, R., et al. (2010). Holocene earthquake record offshore Portugal (SW Iberia): Testing turbidite paleoseismology in a slow-convergence margin. *Quaternary Science Reviews*, *29*(9–10), 1156–1172. https://doi.org/10.1016/j.quascirev.2010.01.010

Harlan, W. S., Claerbout, J. F., & Rocca, F. (1984). Signal/noise separation and velocity estimation. *Geophysics*, *49*(11), 1869–1880. https://doi.org/10.1190/1.1441600

Karstens, J., Berndt, C., Urlaub, M., Watt, S. F., Micallef, A., Ray, M., et al. (2019). From gradual spreading to catastrophic collapse—Reconstruction of the 1888 Ritter Island volcanic sector collapse from high-resolution 3D seismic data. *Earth and Planetary Science Letters*, *517*, 1–13. https://doi.org/10.1016/j.epsl.2019.04.009

Kessinger, W. (1992). Extended split-step Fourier migration. In *SEG Technical Program Expanded Abstracts 1992* (pp. 917–920). Tulsa, OK: Society of Exploration Geophysicists. https://doi.org/10.1190/1.1822254

Khaidukov, V., Landa, E., & Moser, T. (2004). Diffraction imaging by focusing–defocusing: An outlook on seismic superresolution. *Geophysics*, *69*(6), 1478–1490. https://doi.org/10.1190/1.1836821

Klem-Musatov, K., Hoeber, H., Pelissier, M., & Moser, T. J. (Eds.). (2016). *Seismic diffraction*. Tulsa, OK: Society of Exploration Geophysicists. https://doi.org/10.1190/1.9781560803188

Lackey, J., Moore, G., & Strasser, M. (2018). Three-dimensional mapping and kinematic characterization of mass transport deposits along the outer Kumano Basin and Nankai accretionary wedge, southwest Japan. *Progress in Earth and Planetary Science*, *5*(1), 65. https://doi.org/10.1186/s40645-018-0223-4

Leynaud, D., Mulder, T., Hanquiez, V., Gonthier, E., & Régert, A. (2017). Sediment failure types, preconditions and triggering factors in the Gulf of Cadiz. *Landslides*, *14*(1), 233–248. https://doi.org/10.1007/s10346-015-0674-2

Lo Iacono, C., Gràcia, E., Zaniboni, F., Pagnoni, G., Tinti, S., Bartolome, R., et al. (2012). Large, deepwater slope failures: Implications for landslide-generated tsunamis. *Geology*, *40*(10), 931–934. https://doi.org/10.1130/G33446.1

Lucente, C. C., & Pini, G. A. (2003). Anatomy and emplacement mechanism of a large submarine slide within a Miocene foredeep in the northern Apennines, Italy: A field perspective. *American Journal of Science*, *303*(7), 565–602. https://doi.org/10.2475/ajs.303.7.565

Lumley, D. E., Claerbout, J. F., & Bevc, D. (1994). Anti-aliased Kirchhoff 3-D migration. In *SEG Technical Program Expanded Abstracts 1994* (pp. 1282–1285). Tulsa, OK: Society of Exploration Geophysicists. https://doi.org/10.1190/1.1822760

Matias, L. M., Cunha, T., Annunziato, A., Baptista, M. A., & Carrilho, F. (2013). Tsunamigenic earthquakes in the Gulf of Cadiz: Fault model and recurrence. *Natural Hazards and Earth System Sciences*, *13*(1), 1–13. https://doi.org/10.5194/nhess-13-1-2013

Medialdea, T., Somoza, L., Pinheiro, L., Fernández-Puga, M., Vázquez, J., León, R., et al. (2009). Tectonics and mud volcano development in the Gulf of Cádiz. *Marine Geology*, *261*(1–4), 48–63. https://doi.org/10.1016/j.margeo.2008.10.007

Moser, T., & Howard, C. (2008). Diffraction imaging in depth. *Geophysical Prospecting*, *56*(5), 627–641. https://doi.org/10.1111/j.1365-2478.2007.00718.x

Mulder, T., & Cochonat, P. (1996). Classification of offshore mass movements. *Journal of Sedimentary Research*, *66*(1), 43–57. https://doi.org/10.1306/D42682AC-2B26-11D7-8648000102C1865D

Mulder, T., Gonthier, E., Lecroart, P., Hanquiez, V., Marches, E., & Voisset, M. (2009). Sediment failures and flows in the Gulf of Cadiz (eastern Atlantic). *Marine and Petroleum Geology*, *26*(5), 660–672. https://doi.org/10.1016/j.marpetgeo.2008.02.009

Piper, D. J. W., Cochonat, P., & Morrison, M. L. (1999). The sequence of events around the epicentre of the 1929 Grand Banks earthquake: Initiation of debris flows and turbidity current inferred from sidescan sonar. *Sedimentology*, *46*(1), 79–97. https://doi.org/10.1046/j.1365-3091.1999.00204.x

Piper, D. J. W., Pirmez, C., Manley, P. L., Long, D., Flood, R. D., Normark, W. R., & Showers, W. (1997). Mass-transport deposits of the Amazon fan. *Proceedings of the Ocean Drilling Program, Scientific Results*, *155*, 109–146.

Posamentier, H. W., & Martinsen, O. J. (2011). The character and genesis of submarine mass-transport deposits: Insights from outcrop and 3D seismic data. In R. C. Shipp, P. Weimer, & H. W. Posamentier (Eds.), *Mass-Transport Deposits in Deepwater Settings*. Tulsa, OK: SEPM (Society for Sedimentary Geology). https://doi.org/10.2110/sepmsp.096.007

Preine, J., Schwarz, B., Bauer, A., & Hübscher, C. (2020). When there is no offset: A demonstration of seismic diffraction imaging and depth-velocity model building in the Southern Aegean Sea. *Journal of Geophysical Research: Solid Earth*, *125*, e2020JB019961. https://doi.org/10.1029/2020JB019961

Prior, D. B., Bornhold, B. D., & Johns, M. W. (1984). Depositional characteristics of a submarine debris flow. *The Journal of Geology*, *92*(6), 707–727. https://doi.org/10.1086/628907

Reshef, M., & Landa, E. (2009). Post-stack velocity analysis in the dip-angle domain using diffractions. *Geophysical Prospecting*, *57*(5), 811–821. https://doi.org/10.1111/j.1365-2478.2008.00773.x

Satake, K. (2012). Tsunamis generated by submarine landslides. In Y. Yamada, K. Kawamura, K. Ikehara, Y. Ogawa, R. Urgeles, D. Mosher, et al. (Eds.), *Submarine Mass Movements and their Consequences* (pp. 475–484). Dordrecht, the Netherlands: Springer. https://doi.org/10.1007/978-94-007-2162-3_42

Sawyer, D. E., Flemings, P. B., Dugan, B., & Germaine, J. T. (2009). Retrogressive failures recorded in mass transport deposits in the Ursa Basin, Northern Gulf of Mexico. *Journal of Geophysical Research*, *114*, B10102. https://doi.org/10.1029/2008JB006159

Schwarz, B. (2019a). Coherent wavefield subtraction for diffraction separation. *Geophysics*, *84*(3), V157–V168. https://doi.org/10.1190/geo2018-0368.1

Schwarz, B. (2019b). An introduction to seismic diffraction. In C. Schmelzbach (Ed.), Recent advances in seismology (Vol. 60, pp. 1–64) Amsterdam: Elsevier. https://doi.org/10.1016/bs.agph.2019.05.001

Schwarz, B., & Gajewski, D. (2017). Accessing the diffracted wavefield by coherent subtraction. *Geophysical Journal International*, *211*(1), 45–49. https://doi.org/10.1093/gji/ggx291

Schwarz, B., & Krawczyk, C. M. (2020). Coherent diffraction imaging for enhanced fault and fracture network characterization. *Solid Earth*, *11*(5), 1891–1907. https://doi.org/10.5194/se-11-1891-2020

Shipp, R. C., Nott, J. A., & Newlin, J. A. (2004). Physical characteristics and impact of mass transport complexes on deepwater jetted conductors and suction anchor piles. In *Offshore Technology Conference*. Houston, TX: Offshore Technology Conference. https://doi.org/10.4043/16751-MS

Silva, P., Roque, C., Drago, T., Belén, A., Henry, B., Gemma, E., et al. (2020). Multidisciplinary characterization of Quaternary mass movement deposits in the Portimão Bank (Gulf of Cadiz, SW Iberia). *Marine Geology*, *420*, 106086. https://doi.org/10.1016/j.margeo.2019.106086

Sobiesiak, M. S., Kneller, B., Alsop, G. I., & Milana, J. P. (2016). Internal deformation and kinematic indicators within a tripartite mass transport deposit, NW Argentina. *Sedimentary Geology*, *344*, 364–381. https://doi.org/10.1016/j.sedgeo.2016.04.006

Steventon, M. J., Jackson, C. A.-L., Hodgson, D. M., & Johnson, H. D. (2019). Strain analysis of a seismically imaged mass-transport complex, offshore Uruguay. *Basin Research*, *31*(3), 600–620. https://doi.org/10.1111/bre.12337

Stolt, R. H. (1978). Migration by Fourier transform. *Geophysics*, *43*(1), 23–48. https://doi.org/10.1190/1.1440826

Talling, P. J., Wynn, R. B., Schmmidt, D. N., Rixon, R., Sumner, E., & Amy, L. (2010). How did thin submarine debris flows carry boulder-sized intraclasts for remarkable distances across low gradients to the far reaches of the Mississippi fan? *Journal of Sedimentary Research*, *80*(10), 829–851. https://doi.org/10.2110/jsr.2010.076

Taner, M., Fomel, S., & Landa, E. (2006). Separation and imaging of seismic diffractions using plane-wave decomposition. In *SEG Technical Program Expanded Abstracts 2006* (pp. 2401–2405). Tulsa, OK: Society of Exploration Geophysicists. https://doi.org/10.1190/1.2370017

Tappin, D. R., Watts, P., McMurtry, G. M., Lafoy, Y., & Matsumoto, T. (2001). The Sissano, Papua New Guinea tsunami of July 1998—Offshore evidence on the source mechanism. *Marine Geology*, *175*(1), 1–23. https://doi.org/10.1016/S0025-3227(01)00131-1

Terrinha, P., Pinheiro, L., Henriet, J.-P., Matias, L., Ivanov, M., Monteiro, J., et al. (2003). Tsunamigenic–seismogenic structures, neotectonics, sedimentary processes and slope instability on the southwest Portuguese Margin. *Marine Geology*, *195*(1–4), 55–73. https://doi.org/10.1016/S0025-3227(02)00682-5

Urgeles, R., & Camerlenghi, A. (2013). Submarine landslides of the Mediterranean Sea: Trigger mechanisms, dynamics, and frequency-magnitude distribution. *Journal of Geophysical Research: Earth Surface*, *118*, JF002720. https://doi.org/10.1002/2013JF002720

Urgeles, R., INSIGHT Leg 2 Cruise Shipboard Participants, (2019). ImagiNg large SeismogenIc and tsunamiGenic structures of the Gulf of Cadiz with ultra-High resolution Technologies (INSIGHT). Leg 2 Survey Cruise Report (Tech. Rep.). Barcelona: Institute of Marine Sciences.

Urgeles, R., Masson, D. G., Canals, M., Watts, A. B., & Bas, T. L. (1999). Recurrent large-scale landsliding on the west flank of La Palma, Canary Islands. *Journal of Geophysical Research*, *104*(B11), 25331–25348. https://doi.org/10.1029/1999JB900243

Vizcaino, A., Gràcia, E., Pallàs, R., Garcia-Orellana, J., Casas, D., Willmott, V., et al. (2006). Sedimentology, physical properties and age of mass transport deposits associated with the Marquês de Pombal Fault, Southwest Portuguese Margin. *Norwegian Journal of Geology*, *86*(3), 177–186.

Weimer, P., & Shipp, C. (2004). Mass transport complex: Musing on past uses and suggestions for future directions. In *Offshore Technology Conference*. Houston, TX: Offshore Technology Conference. https://doi.org/10.4043/16752-MS

Yilmaz, O. (2001). *Seismic data analysis: Processing, inversion, and interpretation of seismic data*. Tulsa, OK: Society of Exploration Geophysicists. https://doi.org/10.1190/1.9781560801580

Zitellini, N., Gràcia, E., Matias, L., Terrinha, P., Abreu, M., DeAlteriis, G., et al. (2009). The quest for the Africa–Eurasia plate boundary west of the Strait of Gibraltar. *Earth and Planetary Science Letters*, *280*(1–4), 13–50. https://doi.org/10.1016/j.epsl.2008.12.005

Zitellini, N., Rovere, M., Terrinha, P., Chierici, F., & Matias, L. (2004). Neogene through quaternary tectonic reactivation of SW Iberian passive margin. *Pure and Applied Geophysics*, *161*(3), 565–587. https://doi.org/10.1007/s00024-003-2463-4